

# Interleukin-1 prevents SARS-CoV-2-induced membrane fusion to restrict viral transmission via induction of actin bundles

Xu Zheng, Shi Yu, Yanqiu Zhou, Kuai Yu, Yuhui Gao, Mengdan Chen, Dong Duan, Yunyi Li, Xiaoxian Cui, Jiabin Mou, Yuying Yang, Xun Wang, Min Chen ✉, Yaming Jiu ✉, Jincun Zhao ✉, Guangxun Meng ✉

The Center for Microbes, Development and Health, Key Laboratory of Immune Response and Immunotherapy, Shanghai Institute of Immunity and Infection, Chinese Academy of Sciences, University of Chinese Academy of Sciences, Shanghai, 200031, China • Shanghai Municipal Center for Disease Control and Prevention, Shanghai, 200336, China • The First Affiliated Hospital of Guangzhou Medical University, State Key Laboratory of Respiratory Disease, National Clinical Research Center for Respiratory Disease, Guangzhou Institute of Respiratory Health, Guangzhou, 510182, China • Pasteurien College, Soochow University, Suzhou, Jiangsu, 215006, China • Shanghai Blood Center, Shanghai, 200051, China

 [https://en.wikipedia.org/wiki/Open\\_access](https://en.wikipedia.org/wiki/Open_access)

 Copyright information

## Abstract

Innate immune responses triggered by severe acute respiratory syndrome coronavirus 2 (SARS-CoV-2) infection play pivotal roles in the pathogenesis of COVID-19, while host factors including pro-inflammatory cytokines are critical for viral containment. By utilizing quantitative and qualitative models, we discovered that soluble factors secreted by human monocytes potently inhibit SARS-CoV-2-induced cell-cell fusion in viral-infected cells. Through cytokine screening, we identified that interleukin-1 $\beta$  (IL-1 $\beta$ ), a key mediator of inflammation, inhibits syncytia formation mediated by various SARS-CoV-2 strains. Mechanistically, IL-1 $\beta$  activates RhoA/ROCK signaling through a non-canonical IL-1 receptor-dependent pathway, which drives the enrichment of actin bundles at the cell-cell junctions that prevents syncytia formation. Notably, *in vivo* infection experiment in mice confirms that IL-1 $\beta$  significantly restricted SARS-CoV-2 spreading in the lung epithelia. Together, by revealing the function and underlying mechanism of IL-1 $\beta$  on SARS-CoV-2-induced cell-cell fusion, our study highlights an unprecedented antiviral function for cytokines during viral infection.

### eLife assessment

This study provides **valuable** insights into how IL-1 cytokines may protect cells against SARS-CoV-2 infection. By inducing a non-canonical RhoA/ROCK signaling pathway, IL-1beta appears to inhibit the ability of SARS-CoV-2 infected cells to fuse with uninfected cells and produce syncytia. The evidence underlying the identification of the key signaling components required for this inhibitory phenotype in vitro is **solid** and could be further improved by addressing key weaknesses. However, data supporting this specific mechanism of inhibition in IL-1-mediated control of SARS-CoV-2 infection in vivo remains **incomplete**.

<https://doi.org/10.7554/eLife.98593.1.sa2>

## Introduction

The COVID-19 pandemic caused by severe acute respiratory syndrome coronavirus 2 (SARS-CoV-2) infection has spread globally, with at least 755 million people diagnosed and the death toll is over 6.8 million. SARS-CoV-2 variants of concern, including Alpha, Beta, Delta, and Omicron, continue to evolve and increase transmissibility and the ability to escape host immune responses. These variants have brought huge challenges to the design and development of vaccines and therapeutic reagents (Zhou et al., 2020 [↗](#)). In order to discover novel strategies to control the virus, it is important to understand host responses to SARS-CoV-2 infection.

SARS-CoV-2 infection induces cell-cell fusion (also known as syncytia formation) in multiple cell types including lung epithelial cells, neurons and glia (Martínez-Mármol et al., 2023 [↗](#)). Syncytia of SARS-CoV-2 infected cells with neighboring cells could potentially contribute to increased viral transmission and pathogenicity in the infected host (Rajah, Bernier, Buchrieser, & Schwartz, 2022 [↗](#)), which also makes the virus insensitive to extracellular neutralizing antibodies (Li et al., 2022 [↗](#); Yu et al., 2023 [↗](#)). Moreover, syncytia formation among pneumocytes with long-term persistence of viral RNA has been observed in the lung autopsy of deceased COVID-19 donors, which may contribute to prolonged clearance of the virus and long COVID symptoms (Bussani et al., 2020 [↗](#)). Therefore, inhibiting syncytia formation is critical to ensure viral clearance and to control viral transmission.

It has been reported that SARS-CoV-2 mediated syncytia formation is effectively inhibited by multiple interferon (IFN)-stimulating genes (ISGs) (Pfaender et al., 2020 [↗](#); Wang et al., 2020 [↗](#)). However, low IFN levels with impaired ISG responses were observed during early SARS-CoV-2 infection, which may have compromised the antiviral responses of IFN in severe COVID-19 patients (Blanco-Melo et al., 2020 [↗](#); Hadjadj et al., 2020 [↗](#)). Thus, identifying endogenous host factors that regulate syncytia formation is of great significance for harnessing the transmission of SARS-CoV-2.

Of note, a variety of cells are involved in the host responses to SARS-CoV-2 infection (Ren et al., 2021 [↗](#)), lung epithelial cells are the primary target of SARS-CoV-2 infection and transmission, which subsequently recruit and activate innate immune cells (Barnett et al., 2023 [↗](#)). Tissue-resident macrophages and circulating monocytes contribute to local and systemic inflammation largely through releasing inflammatory cytokines (Sefik et al., 2022 [↗](#)). Among these cytokines induced by SARS-CoV-2 infection, the combination of TNF- $\alpha$  and IFN- $\gamma$  induces inflammatory cell death, resulting in clear tissue damage, while other cytokines' function remains obscure (Karki et al., 2021 [↗](#)). In addition, when corticosteroids were used to suppress the inflammatory response in

patients infected by SARS-CoV (N. Lee et al., 2004 [↗](#)) or MERS-CoV (Arabi et al., 2018 [↗](#)), the clearance of viral RNA was obviously delayed, suggesting the importance of innate immune factors including cytokines in viral clearance.

Innate immune cells express toll-like receptors (TLRs), and TLR-mediated signaling induces robust production of inflammatory cytokines (Medzhitov, 2001 [↗](#)). In the current work, we screened the role of soluble pro-inflammatory cytokines on the SARS-CoV-2 spike-induced cell-cell fusion. Notably, we identified that IL-1 $\beta$ , which is the key factor of inflammatory response, inhibited SARS-CoV-2 spike-induced syncytia formation in various cells by activating RhoA/ROCK pathway to initiate actin bundle formation at cell-cell interface between SARS-CoV-2 infected cells and neighboring cells. Importantly, IL-1 $\beta$  significantly reduced SARS-CoV-2 transmission among lung epithelia in experimental mice *in vivo*. Therefore, our data highlight an important role for pro-inflammatory cytokines against viral infection.

## Results

### Host factors secreted by activated innate immune cells inhibit SARS-CoV-2 induced cell-cell fusion

We have previously established quantitative and qualitative models for SARS-CoV-2 spike-induced cell-cell fusion by bioluminescence assay, immunoblotting and fluorescence imaging (Yu et al., 2022 [↗](#)). In order to explore the potential effect of cytokines on SARS-CoV-2-induced cell-cell fusion, human monocyte cell line THP-1 and human peripheral blood mononuclear cells (PBMCs) were used in this study. We applied several TLR ligands to stimulate such innate immune cells and collected the cell culture supernatants for subsequent experiments (**Fig. 1A** [↗](#)). Of note, cell culture supernatants of THP-1 cells stimulated by TLR ligands significantly reduced the bioluminescence signal, while neither untreated THP-1 cell culture supernatant nor the medium control had any effect on the bioluminescence signal reflecting cell-cell fusion (**Fig. 1B** [↗](#)). SARS-CoV-2 spike engagement of ACE2 primed the cleavage of S2' fragment in target cells, a key proteolytic event coupled with spike-mediated membrane fusion (Yu et al., 2022 [↗](#)). In parallel with bioluminescence assay, a large amount of enriched S2' cleavage was detected in HEK293T-Spike and HEK293T-ACE2 co-cultured group and co-culture incubated with untreated THP-1 cell culture supernatant, while S2' cleavage was significantly reduced upon treatment with TLR ligands-stimulated THP-1 cell culture supernatants (**Fig. 1C** [↗](#)). Syncytia formation was also visualized using cells co-expressing spike and a ZsGreen fluorescent reporter. The number and area of syncytium were significantly reduced by the treatment with TLR ligands-stimulated THP-1 cell culture supernatants (**Fig. 1D** [↗](#)). Considering the presence of TLR ligands in cell culture supernatant, we tested their potential direct effects. As expected, TLR ligands alone did not reduce the bioluminescence signal and S2' cleavage compared to the control groups (**Fig. S1 A and B**), as well as no effect on syncytia formation (**Fig. S1C**).

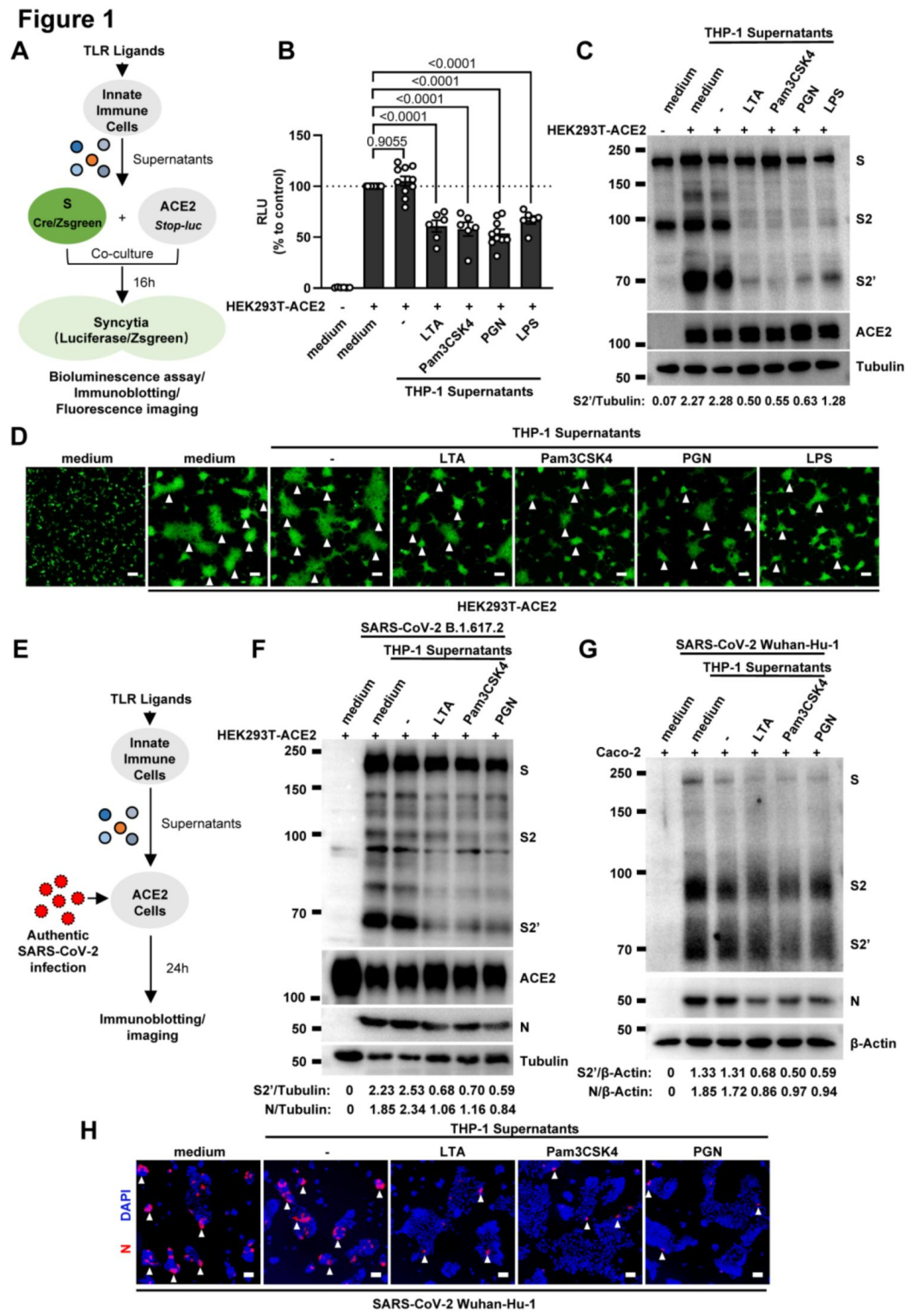


Fig. 1.

## Host factors secreted by activated innate immune cells inhibit SARS-CoV-2 induced cell-cell fusion.

(A) Schematics of the cell-cell fusion model used to quantify spike-mediated syncytium formation upon treatment with cell culture supernatants from TLR ligands stimulated innate immune cells. Cells co-expressing SARS-CoV-2 spike and Cre, were co-cultured with ACE2 and *Stop-luc* co-expressing HEK293T cells for 16 hours, before cell lysates were collected for bioluminescence assay and immunoblotting. Cells co-expressing SARS-CoV-2 spike and ZsGreen, were co-cultured with ACE2 expressing HEK293T cells for 16 hours before fluorescence imaging. (B) Luciferase activity (RLU) measured from HEK293T cell lysates collected from THP-1 supernatants treated HEK293T-S and HEK293T-ACE2 described in (A) for 16 hours. FBS free RPMI 1640 served as medium control group. Data are representative of six individual repeats and displayed as individual points with mean  $\pm$  standard error of the mean (SEM). (C) Immunoblots showing full-length spike, S2, cleaved S2' and ACE2 collected from THP-1 supernatants treated HEK293T-S and HEK293T-ACE2 described in (A) for 16 hours. Blots are representative of three independent experiments. Numbers below the blots indicated the ratio of S2' versus Tubulin. (D) Representative fluorescent image captured at 488 nm from THP-1 supernatants treated HEK293T-S-ZsGreen and HEK293T-ACE2 for 16 hours. (E) Schematic presentation of THP-1 supernatants pre-treatment on authentic SARS-CoV-2 infected cells. Pre-treatment of HEK293T-ACE2 cells with THP-1 supernatants for 1 hour, then inoculated with 0.5 multiplicity of infection (MOI) Delta or WT authentic SARS-CoV-2 (B.1.617.2 and Wuhan-Hu-1) virus. Imaging was performed at 24 hours post-infection (hpi) before cell lysates were harvested for immunoblotting. (F) Immunoblots of Delta SARS-CoV-2 S, S2, cleaved S2', N and ACE2 proteins collected from HEK293T-ACE2 cells 24 hpi as described in (E). Blots are representative of three individual experiments. Numbers below the blots indicated the ratio of S2' or N versus Tubulin. (G) Immunoblots of WT SARS-CoV-2 S, S2, cleaved S2' and N proteins collected from Caco-2 cells 24 hpi as described in (E). Blots are representative of three individual experiments. Numbers below the blots indicated the ratio of S2' or N versus  $\beta$ -Actin. (H) Immunofluorescent images showing morphology of SARS-CoV-2 infected Caco-2 cells pre-treated with THP-1 supernatants. Anti-SARS-CoV-2 N was stained with Alexa fluor 555 and nuclei were counterstained with DAPI respectively. White arrow heads in (D and H) indicate syncytia formation or infected cells, scale bars are indicative of 50  $\mu$ m and images are representative of three independent experiments.

Concurrently, we also tested the effect of PBMCs culture supernatants on SARS-CoV-2 spike-induced cell-cell fusion. Consistent with the results from THP-1 cells, TLR ligands stimulated PBMCs culture supernatants treatment also significantly reduced the bioluminescence signal, S2' cleavage, and the number and area of syncytium compared with the medium group (Fig. S1 D-F). These results suggested that activated innate immune cells released host factors to inhibit SARS-CoV-2 spike-induced cell-cell fusion.

To validate the effect of innate immune cell culture supernatants on cell-cell fusion in authentic SARS-CoV-2 infection, we pre-treated ACE2-expressing cells with THP-1 cell culture supernatants before inoculation with SARS-CoV-2 B.1.617.2 (Delta) or Wuhan-Hu-1 (wild type, WT) strains. Cell lysates were used for the detection of SARS-CoV-2 spike and N protein 24 hours post infection (hpi) (Fig. 1E). This experiment revealed that TLR ligands stimulated THP-1 cell culture supernatants reduced S2' cleavage and N protein during Delta or WT SARS-CoV-2 infection in HEK293T-ACE2 cells, while untreated THP-1 cell culture supernatant had no effect (Fig. 1F and Fig. S2A). In addition, TLR ligands stimulated THP-1 cell culture supernatants significantly reduced the number and area of syncytium induced by Delta or WT SARS-CoV-2 infection (Fig. S2 B and C). Furthermore, we infected the human colon epithelial carcinoma cell line Caco-2 with WT SARS-CoV-2, and found that S2' cleavage and N protein were reduced after TLR ligands stimulated THP-1 cell culture supernatants pre-treatment (Fig. 1G). Accordingly, immunofluorescent staining also showed that TLR ligands stimulated THP-1 cell culture supernatants significantly reduced the number and area of syncytium during SARS-CoV-2 infection in Caco-2 cells (Fig. 1H). These data suggested that host factors secreted by activated innate immune cells inhibit authentic SARS-CoV-2 induced cell-cell fusion.

## IL-1 $\beta$ inhibits SARS-CoV-2 induced cell-cell fusion

To explore which host factors inhibited SARS-CoV-2 induced cell-cell fusion, we first detected mRNA levels of different cytokines in THP-1 cells stimulated by TLR ligands. It was found that the expression levels of *IL1A*, *IL1B*, *IL6* and *IL8* were significantly increased upon TLR ligands stimulation, while *IL4*, *IL12A*, *IFNA1*, *IFNB1* and *IFNG* mRNA levels were relatively unchanged or undetected (**Fig. S3A**). In addition, we also detected the mRNA levels of cytokine receptors in HEK293T modelling cells, confirming that *IL1R1*, *IL4R*, *IL6ST*, *IL8RA*, *IFNAR1*, *IFNGR1* were expressed in such cells, while *IL2RA* and *IL12RB1* were undetectable (**Fig. S3B**).

We next selected recombinant IL-1 $\alpha$ , IL-1 $\beta$ , IL-6, and IL-8 to test whether individual cytokine may play a role in affecting SARS-CoV-2 spike induced cell-cell fusion (**Fig. 2A**). Interestingly, IL-1 $\alpha$  and IL-1 $\beta$  significantly reduced the bioluminescence signal compared to the control group, while IL-6 and IL-8 had little or no effect (**Fig. 2B**). In addition, fluorescence images of cells expressing ZsGreen reporter also confirmed that IL-1 $\alpha$  and IL-1 $\beta$  significantly inhibited SARS-CoV-2 spike induced syncytia formation (**Fig. S3C**). Furthermore, IL-1 $\beta$  and IL-1 $\alpha$  both reduced the bioluminescence signal and S2' cleavage (**Fig. 2 C and D, and Fig. S4A**) in cell lysates in a dose-dependent manner. Moreover, the syncytia formation was inhibited with increasing concentrations of IL-1 $\beta$  or IL-1 $\alpha$  (**Fig. S4 B and C**). Intriguingly, when we added both IL-1 $\alpha$  and IL-1 $\beta$ , there was no synergistic inhibition on cell-cell fusion compared to either cytokine alone (**Fig. S4 D and E**), suggesting a potential saturation of IL-1 receptor binding to these homologues. Since both IL-1 $\alpha$  and IL-1 $\beta$  activate the downstream pathway through the same receptor IL-1R1, it is suggested that IL-1 $\alpha$  or IL-1 $\beta$  may inhibit cell-cell fusion through the same pathway. Considering the higher mRNA level of *IL1B* than *IL1A*, as well as the classical release pathway of IL-1 $\beta$  from innate immune cells (Weber, Wasiliew, & Kracht, 2010), we mainly used IL-1 $\beta$  for further experiments.



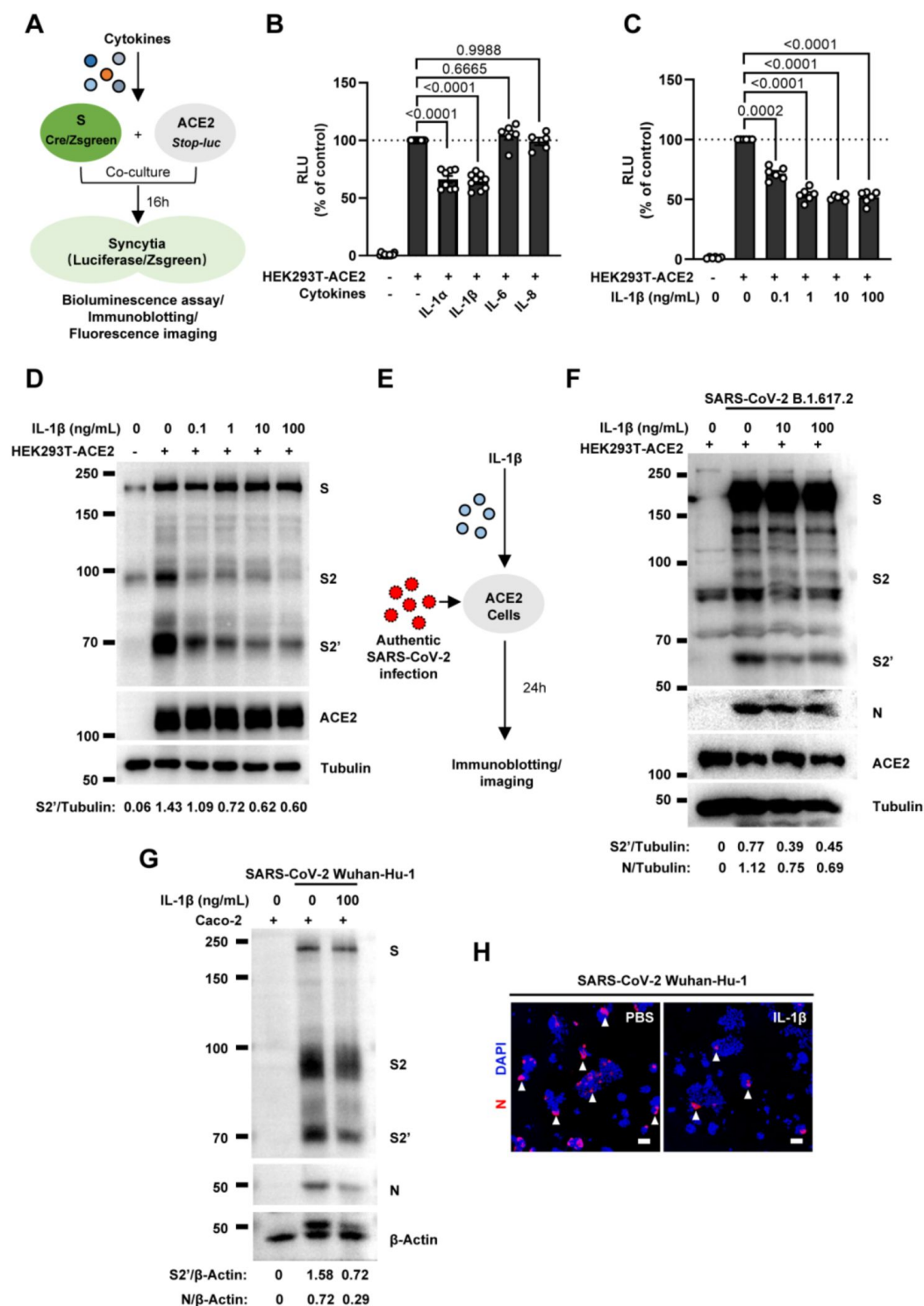


**Fig. 2.**

### IL-1 $\beta$ inhibits SARS-CoV-2 induced cell-cell fusion.

(A) Schematics of the cell-cell fusion model used to quantify spike-mediated syncytium formation upon treatment with different cytokines. Cells co-expressing SARS-CoV-2 spike and Cre, were co-cultured with ACE2 and *Stop-luc* co-expressing HEK293T cells for 16 hours, before cell lysates were collected for bioluminescence assay and immunoblotting. Cells co-expressing SARS-CoV-2 spike and ZsGreen, were co-cultured with ACE2 expressing HEK293T

cells for 16 hours before fluorescence imaging. **(B)** Luciferase activity (RLU) measured from HEK293T cell lysates collected from different cytokines treated HEK293T-S and HEK293T-ACE2 described in (A) for 16 hours. IL-1 $\alpha$  (10 ng/mL), IL-1 $\beta$  (1 ng/mL), IL-6 (100 ng/mL) or IL-8 (100 ng/mL) were added into the cell-cell fusion system. Data are representative of six individual repeats and displayed as individual points with mean  $\pm$  standard error of the mean (SEM). **(C)** Luciferase activity (RLU) measured from HEK293T cell lysates collected from different concentrations of IL-1 $\beta$  treated HEK293T-S and HEK293T-ACE2 for 16 hours. Data are representative of six individual repeats and displayed as individual points with mean  $\pm$  standard error of the mean (SEM). **(D)** Immunoblots showing full-length spike, S2, cleaved S2' and ACE2 collected from different concentrations of IL-1 $\beta$  treated HEK293T-S and HEK293T-ACE2 for 16 hours. Blots are representative of three independent experiments. Numbers below the blots indicated the ratio of S2' versus Tubulin. **(E)** Schematic presentation of IL-1 $\beta$  pre-treatment on authentic SARS-CoV-2 infected cells. Pre-treatment of HEK293T-ACE2 cells with different concentrations of IL-1 $\beta$  for 1 hour, then inoculated with 0.5 MOI Delta or WT authentic SARS-CoV-2 (B.1.617.2 and Wuhan-Hu-1) virus. Brightfield images were captured at 24 hours post-infection (hpi) before cell lysates were harvested for immunoblotting. **(F)** Immunoblots of Delta SARS-CoV-2 S, S2, cleaved S2', N and ACE2 proteins collected from HEK293T-ACE2 cells 24 hpi as described in (E). Blots are representative of three individual experiments. Numbers below the blots indicated the ratio of S2' or N versus Tubulin. **(G)** Immunoblots of WT SARS-CoV-2 S, S2, cleaved S2' and N proteins collected from Caco-2 cells 24 hpi as described in (E). Blots are representative of three individual experiments. Numbers below the blots indicated the ratio of S2' or N versus  $\beta$ -Actin. **(H)** Immunofluorescent images showing morphology of SARS-CoV-2 infected Caco-2 cells pre-treated with or without IL-1 $\beta$ . Anti-SARS-CoV-2 N was stained with Alexa fluor 555 and nuclei were counterstained with DAPI respectively. White arrow heads indicate syncytia formation or infected cells, scale bars are indicative of 50  $\mu$ m and images are representative of three independent experiments.

In order to validate the effect of IL-1 $\beta$  on cell-cell fusion during authentic SARS-CoV-2 infection, we pre-treated ACE2-expressing cells with IL-1 $\beta$  before inoculating with Delta or WT authentic SARS-CoV-2. Cell lysates were used for the detection of SARS-CoV-2 spike and N protein 24 hpi (**Fig. 2E**). To this end, it was found that IL-1 $\beta$  reduced S2' cleavage and N protein compared to the control group during such infection both in HEK293T-ACE2 (**Fig. 2F** and **Fig. S5A**) and Caco-2 cells (**Fig. 2G**). Meanwhile, IL-1 $\beta$  inhibited authentic SARS-CoV-2 induced syncytia formation (**Fig. 2H** and **Fig. S5 B and C**). These results verified that IL-1 $\beta$  inhibits authentic SARS-CoV-2 induced cell-cell fusion in various target cells.

As expected, innate immune cells activated by TLR ligands secreted IL-1 $\beta$  into the cell culture supernatants (**Fig. S6, A and B**), and TLR2 was essential for THP-1 cells to release IL-1 $\beta$  in response to TLR2 ligands (**Fig. S6C**). More importantly, the cell culture supernatants of TLR2-knockout THP-1 cells stimulated by TLR2 Ligands had no effect on the bioluminescence signal, while the cell culture supernatants from WT THP-1 cells stimulated by the same TLR2 Ligands significantly reduced the bioluminescence signal (**Fig. S6D**). In addition, pre-treatment with TAK1 inhibitor (SZ-7) or IKK $\beta$  inhibitor (TPCA1) in WT THP-1 cells prevented IL-1 $\beta$  secretion after PGN stimulation (**Fig. S6E**), as well as eliminated the inhibitory effect of PGN-stimulated WT THP-1 cell culture supernatant on SARS-CoV-2 spike-induced cell-cell fusion (**Fig. S6F**). In parallel, pre-treatment with these inhibitors in PBMCs showed the same results (**Fig. S6 G and H**). These data suggested that TLR-knockout or inhibitors targeting the respective TLR signaling prevented innate immune cells from releasing IL-1 $\beta$  into supernatants, which led to failed inhibition of SARS-CoV-2 spike induced cell-cell fusion. These findings thus further verify that IL-1 $\beta$  is an important host factor inhibiting SARS-CoV-2 induced cell-cell fusion.

To investigate the effector function of IL-1 on cells expressing SARS-CoV-2 spike (donor cells) and neighboring cells expressing ACE2 (acceptor cells), we pre-treated HEK293T-S or HEK293T-ACE2 cells or both with IL-1 $\beta$ , then co-cultured after washing with PBS. Cells were then analyzed by the quantitative and qualitative models (**Fig. S7A**). Notably, pre-treatment of either HEK293T-S or HEK293T-ACE2 cells with IL-1 $\beta$  alone reduced bioluminescence signal and S2' cleavage; when IL-1 $\beta$  pre-treatment on both HEK293T-S and HEK293T-ACE2 cells was applied, bioluminescence signal and S2' cleavage were further reduced (**Fig. S7B**). Furthermore, we used Vero E6-overexpressing



ACE2 cell line (Vero E6-ACE2) and human Calu-3 cells as acceptor cells. In this case, pre-treatment of either HEK293T-S or Vero E6-ACE2 cells with IL-1 $\beta$  alone reduced part of S2' cleavage, while IL-1 $\beta$  pre-treatment of both HEK293T-S and Vero E6-ACE2 cells led to further reduction of S2' cleavage (**Fig. S7C**). And the same results were observed in the case of Calu-3 as acceptor cells (**Fig. S7D**). Accordingly, fluorescence imaging showed that IL-1 $\beta$  significantly reduced the number and area of syncytia (**Fig. S8A**). Notably, IL-1 $\beta$  reduced the bioluminescence signal and S2' cleavage in different SARS-CoV-2 variants (**Fig. S8 B-D**). These results suggest that IL-1 $\beta$  acts on both donor and acceptor cells to inhibit SARS-CoV-2 spike induced cell-cell fusion in various cell lines.

SARS-CoV (Belouzard, Chu, & Whittaker, 2009 [\[1\]](#)) and MERS-CoV (Straus et al., 2020 [\[2\]](#)) spike protein also induce cell-cell fusion in target cells. Therefore, we further explored whether IL-1 $\beta$  could also inhibit SARS-CoV and MERS-CoV spike-induced cell-cell fusion in ACE2-or Dipeptidyl peptidase-4 (DPP4)-expressing cells by bioluminescence assay, immunoblotting and a modified *stop-mCherry* fluorescent model, wherein mCherry reporter is only expressed when Cre excises the Stop cassette inside the fused syncytia (**Fig. S9A**). Similar to SARS-CoV-2 spike-induced cell-cell fusion, IL-1 $\beta$  also reduced bioluminescence signal (**Fig. S9 B and C**), S2' cleavage (**Fig. S9 D and E**) and the number and area of syncytium (**Fig. S9F**). These data suggested that IL-1 $\beta$  possesses a broad spectrum to inhibit cell-cell fusion induced by different coronaviruses.

## IL-1 $\beta$ inhibits SARS-CoV-2 induced cell-cell fusion through IL-1R1/MyD88/IRAK/TRAF6 pathway

To investigate the mechanism of IL-1 $\beta$  inhibition on SARS-CoV-2 induced cell-cell fusion, we performed gene knockout using CRISPR-Cas9 technology, in conjunction with inhibitors targeting the IL-1 receptor pathway (**Fig. 3A** [\[3\]](#)). In the presence of IL-1 receptor antagonist (IL-1RA), IL-1 $\beta$  was unable to reduce bioluminescence signal and S2' cleavage (**Fig. 3B** [\[4\]](#)). MyD88 is the downstream adaptor of IL-1R1. We then generated MyD88 knockout HEK293T cell line, wherein IL-1 $\beta$  was unable to reduce bioluminescence signal (**Fig. 3C** [\[5\]](#)) and S2' cleavage (**Fig. S10A**). In addition, we found that IL-1 $\beta$  was unable to reduce bioluminescence signal and S2' cleavage in the presence of IRAK1/4 inhibitor (**Fig. 3D** [\[6\]](#)). Furthermore, IL-1 $\beta$  was also unable to reduce bioluminescence signal (**Fig. 3E** [\[7\]](#)) and S2' cleavage (**Fig. S10B**) in TRAF6 knockout HEK293T cell line. These results suggested that IL-1 $\beta$  inhibits SARS-CoV-2 spike induced cell-cell fusion through IL-1R1-MyD88-IRAK-TRAF6 pathway.

**Figure 3**

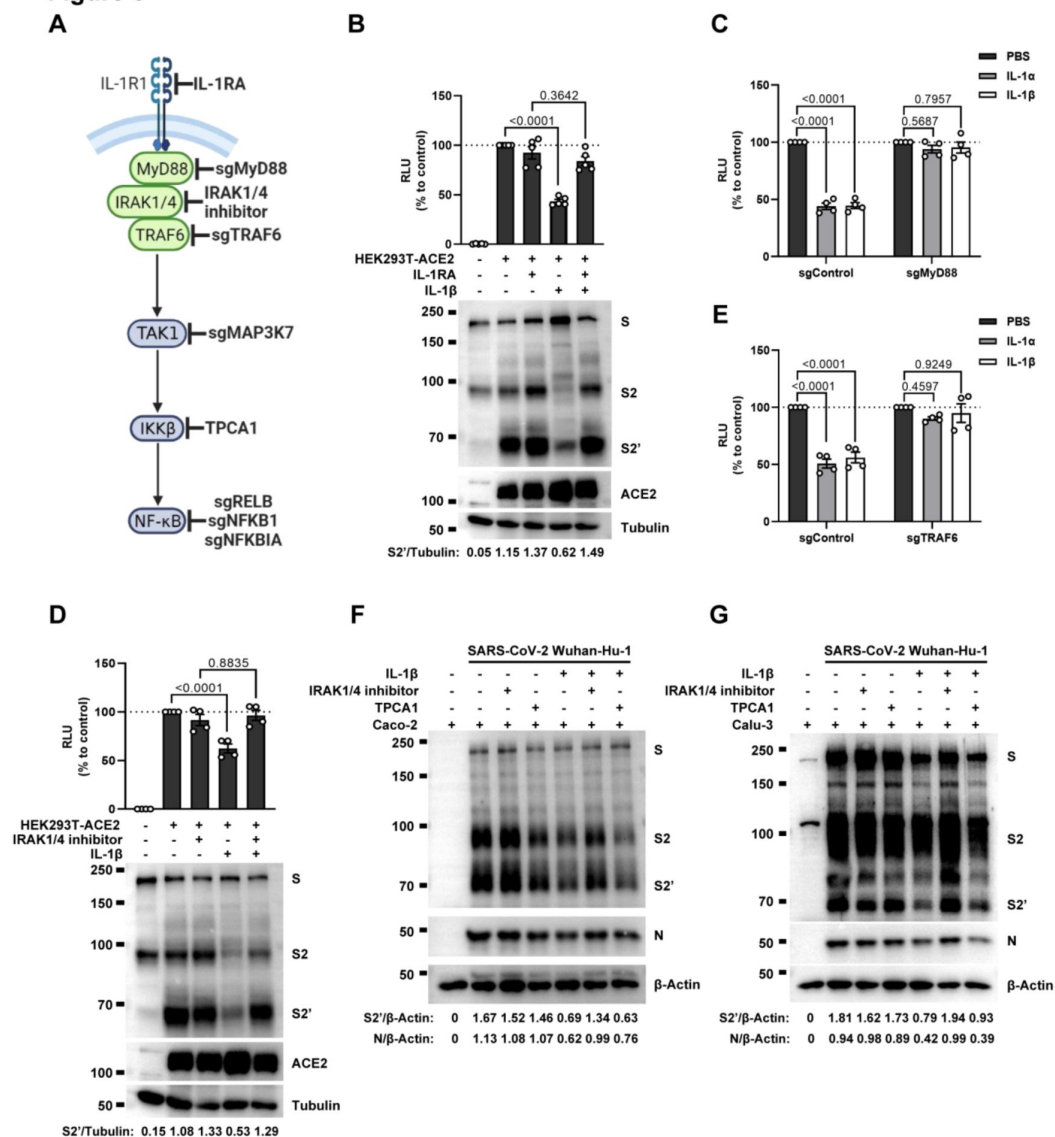


**Fig. 3.**

### IL-1β inhibits SARS-CoV-2 induced cell-cell fusion through IL-1R1/MyD88/IRAK/TRAF6 pathway.

(A) Schematics of gene knockout or inhibitor treatment in the IL-1 receptor pathway. (B) Luciferase activity (RLU) measured from HEK293T cell lysates and immunoblots showing full-length spike, S2, cleaved S2' and ACE2 collected from HEK293T-S and HEK293T-ACE2 pre-treated with 1000 ng/mL IL-1RA for 30 min, then treated with 1 ng/mL IL-1β for 16 hours. Data and blots are representative of five individual repeats. Numbers below the blots indicated the ratio of S2' versus Tubulin. (C) Luciferase activity (RLU) measured from cell lysates collected from 10 ng/mL IL-1α or 1 ng/mL IL-1β treated sgControl or sgMyD88 HEK293T cell-cell fusion system for 16 hours. Data are representative of four individual repeats and displayed as individual points with mean ± standard error of the mean (SEM). (D) Luciferase activity (RLU) measured from HEK293T cell lysates and immunoblots showing full-length spike, S2, cleaved S2' and ACE2 collected from HEK293T-S and HEK293T-ACE2 pre-treated with 2μM IRAK1/4 inhibitor for 30 min, then treated with 1 ng/mL IL-1β for 16 hours. Data and blots are representative of four individual repeats. Numbers below the blots indicated the ratio of S2' versus Tubulin. (E) Luciferase activity (RLU) measured from cell lysates collected from 10 ng/mL IL-1α or 1 ng/mL IL-1β treated sgControl or sgTRAF6 HEK293T cell-cell fusion system for 16 hours.

Data are representative of four individual repeats and displayed as individual points with mean  $\pm$  standard error of the mean (SEM). (F) Immunoblots showing full-length spike, S2, cleaved S2' and ACE2 collected from Caco-2 cells, which pre-treated with 2 $\mu$ M IRAK1/4 inhibitor and 10 ng/mL IL-1 $\beta$  for 1 hour, then infected with authentic SARS-CoV-2 for 24 hours. Blots are representative of three independent experiments. Numbers below the blots indicated the ratio of S2' or N versus  $\beta$ -Actin. (G) Immunoblots showing full-length spike, S2, cleaved S2' and ACE2 collected from Calu-3 cells, which infected with authentic SARS-CoV-2 for 1 hour, then washed with PBS before treated with 2 $\mu$ M IRAK1/4 inhibitor and 10 ng/mL IL-1 $\beta$  for 24 hours. Blots are representative of three independent experiments. Numbers below the blots indicated the ratio of S2' or N versus  $\beta$ -Actin.

Intriguingly, when we tested TAK1, a downstream molecule of TRAF6 for the potential involvement in the signaling, it was found that IL-1 $\beta$  still reduced bioluminescence signal and S2' cleavage in TAK1 knockout (sgMAP3K7) HEK293T cell line (**Fig. S11A**). Moreover, we found that in the presence of TPCA1, an IKK $\beta$  inhibitor, IL-1 $\beta$  still inhibited bioluminescence signal and S2' cleavage as well (**Fig. S11B**). Although IL-1 $\beta$  upregulates the mRNA transcription levels of NF- $\kappa$ B pathway-related genes, such as *RELB*, *NFKBIA*, and *NFKB1* (**Fig. S11C**), IL-1 $\beta$  still reduced the bioluminescence signal after these NF- $\kappa$ B pathway-related genes knockout (**Fig. S11D**). Taken together, these results demonstrated that IL-1 $\beta$  inhibits SARS-CoV-2 spike induced cell-cell fusion independent from the TAK1-IKK $\beta$ -NF- $\kappa$ B signaling cascade.

Furthermore, we validated these findings in authentic SARS-CoV-2 infected Caco-2 and Calu-3 cells. Consist with the results from HEK293T cells, IL-1 $\beta$  failed to reduce S2' cleavage and N protein in the presence of IRAK1/4 inhibitor, whereas it still reduced S2' cleavage and N protein in the presence of the IKK $\beta$  inhibitor TPCA1 in Caco-2 (**Fig. 3F**) and Calu-3 cells (**Fig. 3G**).

## IL-1 $\beta$ inhibits SARS-CoV-2 induced cell-cell fusion through RhoA/ROCK mediated actin bundle formation at the cell-cell junction

It has been reported that IL-1 $\beta$  activates RhoA signaling via MyD88 and IRAK, which is a pathway independent from IKK $\beta$  (Chen, Zuraw, Liu, Huang, & Pan, 2002). As a major downstream effector of RhoA, ROCK phosphorylates substrates that are involved in the regulation of the actin cytoskeleton, cell attachment, and cell motility (Riento & Ridley, 2003). Therefore, we set out to detect the active level of RhoA through pull-down assay. To this end, we verified that IL-1 $\beta$  activated RhoA signaling in sgControl HEK293T cells but not in sgMyD88- or sgTRAF6-HEK293T cells (**Fig. 4A**). To directly visualize the distribution of endogenous GTP-RhoA (active RhoA), we used a location biosensor derived from the carboxy terminus of anillin (GFP-AHPH) (Priya et al., 2015; Sun et al., 2015). Interestingly, IL-1 $\beta$  significantly increased the fluorescence intensity of GFP-AHPH in sgControl HEK293T cells, but had no effect in sgMyD88- and sgTRAF6-HEK293T cells (**Fig. 4B and C**).

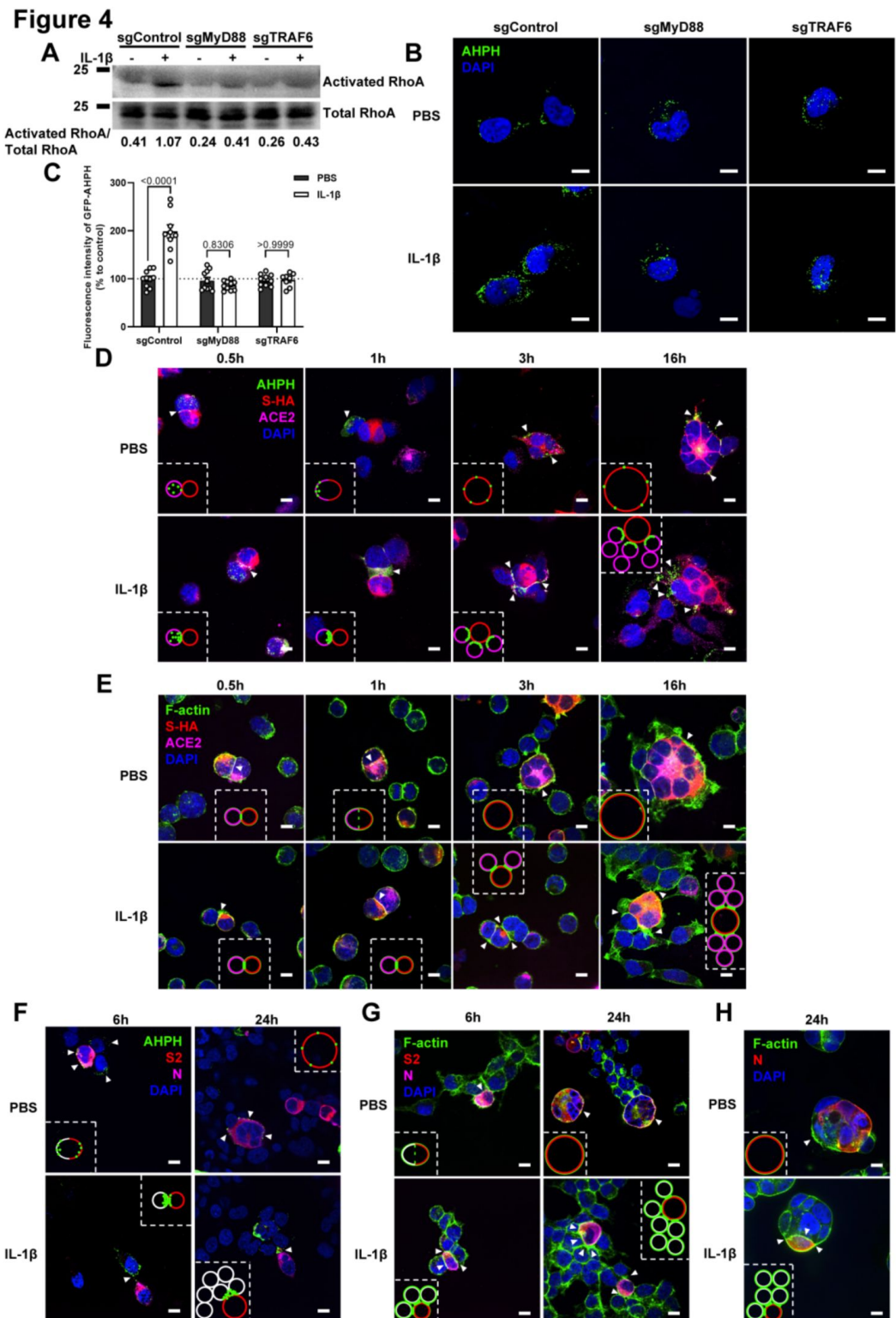


**Fig. 4.**

## IL-1 $\beta$ inhibits SARS-CoV-2 induced cell-cell fusion through RhoA/ROCK mediated actin bundles at cell-cell junction.

(A) GTP-RhoA pull-down assay to detect the active level of RhoA in sgControl, sgMyD88 and sgTRAF6 HEK293T cells after 1 ng/mL IL-1 $\beta$  treatment for 30 min. Immunoblots showing activated RhoA and total RhoA. Blots are representative of three independent experiments. Numbers below the blots indicated the ratio of active RhoA versus total RhoA. (B) Representative confocal images of GFP-AHPH after 1 ng/mL IL-1 $\beta$  treatment for 30 min in sgControl, sgMyD88 and sgTRAF6 HEK293T cells. Scale bars, 10  $\mu$ m. (C) Quantification of fluorescence intensity of GFP-AHPH in (B). Data are representative of eight individual repeats. (D) Representative confocal images of GFP-AHPH localization with or without 1 ng/mL IL-1 $\beta$  treatment at different time points of syncytia formation in HEK293T-S-HA and HEK293T-ACE2 cells. Schematics with green dots in the white dashed line boxes representing GFP-AHPH, red cycles representing S-expressing cells, and magenta cycles representing ACE2-expressing cells. White arrow heads indicate the localization of GFP-AHPH, scale bars, 10  $\mu$ m. Images are representative of three independent experiments. (E) Representative confocal images of F-actin stained with phalloidin-488 in the presence or absence of 1 ng/mL IL-1 $\beta$  treatment at different time points of syncytia formation in HEK293T-S-HA and HEK293T-ACE2 cells. Schematics with green lines in the white dashed line boxes representing actin bundles, red cycles representing S-expressing cells, and magenta cycles representing ACE2-expressing cells. White arrow heads indicate the enrichment or disappearance of F-actin, scale bars, 10  $\mu$ m. Images are representative of three independent experiments. (F) Representative confocal images of GFP-AHPH localization with or without 1 ng/mL IL-1 $\beta$  treatment in 0.5 MOI WT authentic SARS-CoV-2 infected HEK293T-ACE2 cells at 6 hpi and 24 hpi. Schematics with green dots in the white dashed line boxes representing GFP-AHPH, red cycles representing SARS-CoV-2 infected cells, and white cycles representing neighboring cells. White arrow heads indicate the localization of GFP-AHPH, scale bars, 10  $\mu$ m. Images are representative of three independent experiments. (G, H) Representative confocal images of F-actin stained with phalloidin-488 in the presence or absence of 1 ng/mL IL-1 $\beta$  treatment in 0.5 MOI WT authentic SARS-CoV-2 infected HEK293T-ACE2 cells at 6 hpi and 24 hpi (G) or Caco-2 cells at 24 hpi (H). Schematics with green lines in the white dashed line boxes representing actin bundles, red cycles representing SARS-CoV-2 infected cells, and white cycles representing neighboring cells. Scale bars, 10  $\mu$ m. Images are representative of three independent experiments. White arrow heads in (G and H) indicate the enrichment or disappearance of F-actin.

To investigate whether IL-1 $\beta$  inhibits SARS-CoV-2 spike-induced cell-cell fusion through RhoA/ROCK pathway, we co-transfected GFP-AHPH in ACE2-expressing cells, then co-cultured with S-expressing cells at different time points. In the process of syncytia formation, cell-cell contact established between S-expressing cells and ACE2-expressing cells, and GFP-AHPH localized distally from cell-cell junction in the early stage of syncytia formation. With the enlargement of syncytium, GFP-AHPH is visualized at the periphery of syncytium (**Fig. 4D**, [top panel](#)). However, in IL-1 $\beta$  treated group, GFP-AHPH foci is enriched to the cell-cell junction in the early stage. Over time, GFP-AHPH was recruited more to the cell-cell junction between S-expressing cells and ACE2-expressing cells, preventing further cell-cell fusion (**Fig. 4D**, [bottom panel](#)). Cartoon schematics inserted in the imaging data illustrate such findings in a modeled manner.

ROCK-mediated actin rearrangement is through the downstream substrates, which induces cross-linking of actin bundles with myosin and generate contractile forces along these bundles (Watanabe, Kato, Fujita, Ishizaki, & Narumiya, 1999). It has been reported that RhoA initiates actin arc formation (Dupraz et al., 2019; Stern et al., 2021), so we further explored the changes of actin cytoskeleton during SARS-CoV-2 spike-induced cell-cell fusion. Phalloidin staining showed that actin filaments (F-actin) at cell-cell junction between S-expressing cells and ACE2-expressing cells was gradually disappeared along with cell-cell fusion in the early stages of syncytia formation. With the formation and enlargement of syncytium, F-actin of syncytium is preferably distributed peripherally (**Fig. 4E**, [top panel](#)). However, IL-1 $\beta$  activated RhoA to initiate actin bundles formation at cell-cell junction, the formation of these actin bundles potentially generates

barriers and prevents membrane fusion between S-expressing cells and ACE2-expressing cells. Even with the prolonged co-culture time, IL-1 $\beta$ -induced actin bundles formed at cell junctions consistently inhibited further syncytia formation (**Fig. 4E** [↗](#), **bottom panel**).

Consistent with our previous results, immunofluorescence staining showed GFP-AHPH moving to the opposite of cell-cell junction and locating peripherally with syncytia formation (**Fig. 4F** [↗](#), **top panel**), while upon IL-1 $\beta$  treatment, GFP-AHPH located at the cell-cell junction of authentic SARS-CoV-2 infected cells and neighboring cells (**Fig. 4F** [↗](#), **bottom panel**). In parallel, staining results showed that F-actin at the cell-cell junction were disassembled during authentic SARS-CoV-2 infection; with the formation of syncytium, F-actin of syncytium was mainly distributed peripherally (**Fig. 4G** [↗](#), **top panel**). However, actin bundles formed at cell-cell junction induced by IL-1 $\beta$  inhibited membrane fusion and further syncytia formation (**Fig. 4G** [↗](#), **bottom panel**). Furthermore, we also observed the same results in authentic SARS-CoV-2 infected Caco-2 cells. F-actin of syncytium in control group was also distributed peripherally, the formation of syncytium promoted the transmission of SARS-CoV-2, as N protein was widely distributed in the cytoplasm of the syncytium (**Fig. 4H** [↗](#), **top panel**). While in IL-1 $\beta$  treated group, actin bundles formed at cell-cell junction between SARS-CoV-2 infected cells and neighboring cells prevented syncytia formation and further viral transmission (**Fig. 4H** [↗](#), **bottom panel**). Together, these data revealed that IL-1 $\beta$  induced the formation of actin bundles at the cell-cell junction of SARS-CoV-2 infected cells and neighboring cells through RhoA/ROCK pathway, which inhibited SARS-CoV-2 induced cell-cell fusion.

To further investigate the role of RhoA/ROCK pathway in inhibiting SARS-CoV-2 induced cell-cell fusion, we co-transfected constitutively activated RhoA L63 ([Nobes & Hall, 1999](#) [↗](#)) (RhoA-CA) plasmid with spike or ACE2 in HEK293T cells, and found that RhoA-CA significantly reduced the bioluminescence signal and S2' cleavage in a dose-dependent manner (**Fig. 5A** [↗](#)). HEK293T-ACE2 (**Fig. S12A**), Caco-2 (**Fig. 5B** [↗](#)) and Calu-3 cells (**Fig. 5C** [↗](#)) expressing RhoA-CA also significantly reduced S2' cleavage and N protein compared to the control group during authentic SARS-CoV-2 infection. Meanwhile, we observed that constitutive activation of RhoA enriches actin bundles at cell-cell junction, thus preventing SARS-CoV-2 induced cell-cell fusion in HEK293T-ACE2 (**Fig. S12B**), Caco-2 (**Fig. 5D** [↗](#)) and Calu-3 cells (**Fig. 5E** [↗](#)).



**Figure 5**

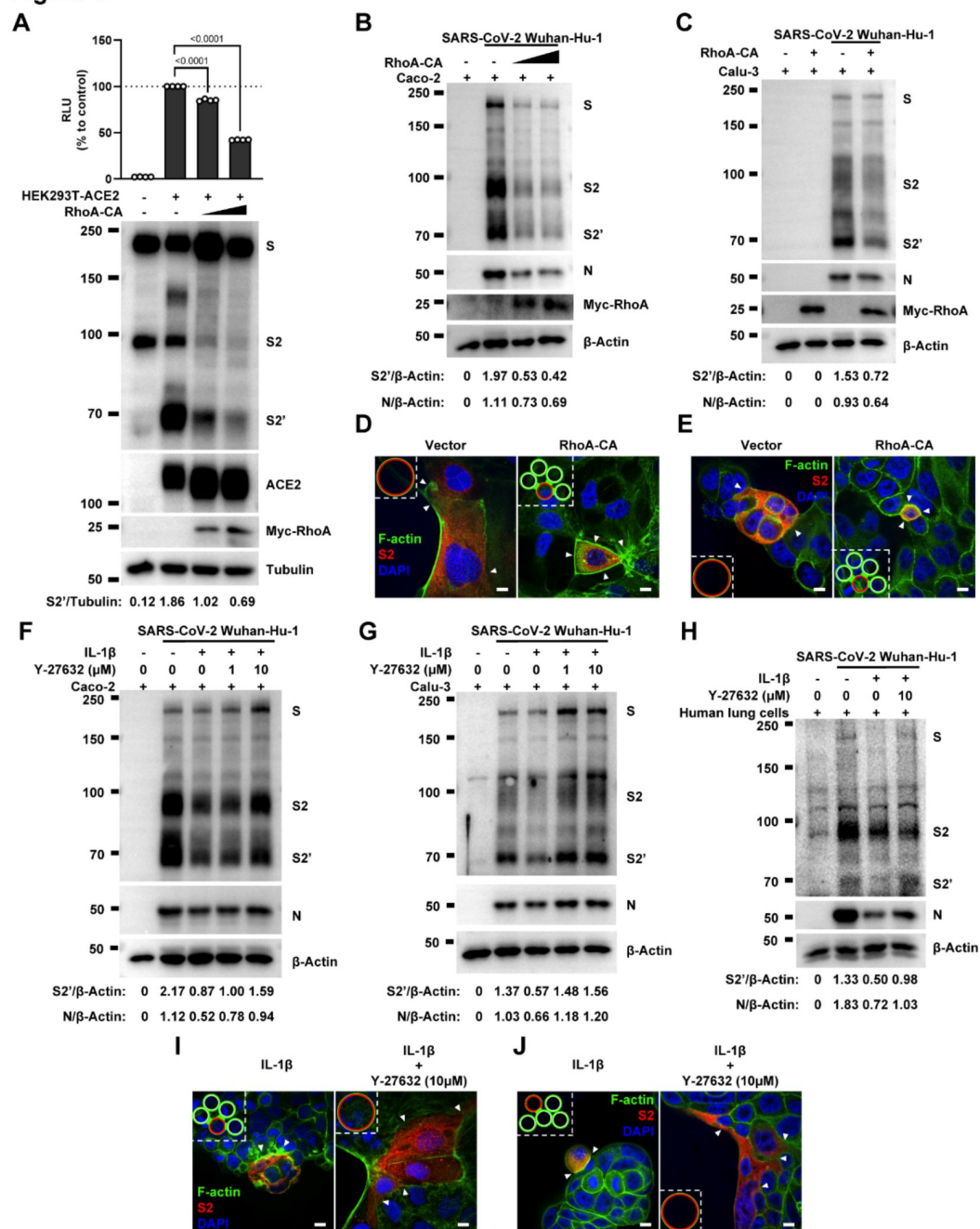


**Fig. 5.**

### Activation of RhoA/ROCK pathway prevents authentic SARS-CoV-2 induced cell-cell fusion by forming actin bundles.

(A) Luciferase activity (RLU) measured from HEK293T cell lysates and immunoblots showing full-length spike, S2, cleaved S2', ACE2 and Myc-RhoA collected from transfected vector, 10 ng or 20 ng constitutively active RhoA mutant (RhoA-CA) both in HEK293T-S and HEK293T-ACE2. Data and blots are representative of four individual repeats. Numbers below the blots indicated the ratio of S2' versus Tubulin. (B) Immunoblots of WT SARS-CoV-2 S, S2, cleaved S2', N and Myc-RhoA collected from Caco-2 cells, which transfected with vector, 10 ng or 20 ng RhoA-CA before infected with 0.5 MOI WT authentic SARS-CoV-2 for 24 hours. Blots are representative of three individual

experiments. Numbers below the blots indicated the ratio of S2' or N versus  $\beta$ -Actin. **(C)** Immunoblots of WT SARS-CoV-2 S, S2, cleaved S2', N and Myc-RhoA collected from lentivirus-transduced Calu-3 cells expressing vector or RhoA-CA, infected with WT authentic SARS-CoV-2 for 24 hours. Blots are representative of three individual experiments. Numbers below the blots indicated the ratio of S2' or N versus  $\beta$ -Actin. **(D)** Representative confocal images of F-actin stained with phalloidin-488 from Caco-2 cells described in (B). Schematics with green lines in the white dashed line boxes representing actin bundles, red cycles representing S-expressing cells. Scale bars, 10  $\mu$ m. Images are representative of four independent experiments. **(E)** Representative confocal images of F-actin stained with phalloidin-488 from Calu-3 cells described in (C). Schematics with green lines in the white dashed line boxes representing actin bundles, red cycles representing S-expressing cells. White arrow heads in (D and E) indicate the enrichment or disappearance of F-actin, scale bars, 10  $\mu$ m. Images are representative of four independent experiments. **(F)** Immunoblots of WT SARS-CoV-2 S, S2, cleaved S2' and N collected from Caco-2 cells, which treated with different concentrations of Y-27632 and 10 ng/mL IL-1 $\beta$  for 1 hour, then infected with 0.5 MOI WT authentic SARS-CoV-2 for 24 hours. Blots are representative of three individual experiments. Numbers below the blots indicated the ratio of S2' or N versus  $\beta$ -Actin. **(G)** Immunoblots of WT SARS-CoV-2 S, S2, cleaved S2' and N collected from Calu-3 cells, which infected with authentic SARS-CoV-2 for 1 hour, then washed with PBS before treated with different concentrations of Y-27632 and 10 ng/mL IL-1 $\beta$  for 24 hours. Blots are representative of three independent experiments. Numbers below the blots indicated the ratio of S2' or N versus  $\beta$ -Actin. **(H)** Immunoblots of WT SARS-CoV-2 S, S2, cleaved S2' and N collected from human lung cells, which infected with authentic SARS-CoV-2 for 1 hour, then washed with PBS before treated with 10  $\mu$ M Y-27632 and 10 ng/mL IL-1 $\beta$  for 24 hours. Blots are representative of three independent experiments. Numbers below the blots indicated the ratio of S2' or N versus  $\beta$ -Actin. **(I)** Representative confocal images of F-actin stained with phalloidin-488 in Caco-2 cells described in (G). Schematics with green lines in the white dashed line boxes representing actin bundles, red cycles representing S-expressing cells. Scale bars, 10  $\mu$ m. Images are representative of four independent experiments. **(J)** Representative confocal images of F-actin stained with phalloidin-488 in Calu-3 cells described in (H). Schematics with green lines in the white dashed line boxes representing actin bundles, red cycles representing S-expressing cells. White arrow heads in (I and J) indicate the enrichment or disappearance of F-actin, scale bars, 10  $\mu$ m. Images are representative of four independent experiments.

ROCK inhibitor Y-27632 treatment prevents the formation of actin bundles (van der Heijden et al., 2008), so we hypothesized that Y-27632 could affect the inhibitory effect of IL-1 $\beta$  on SARS-CoV-2 spike-induced cell-cell fusion. Indeed, Y-27632 treatment increased bioluminescence signal and S2' cleavage in a dose-dependent manner, promoting syncytia formation. When treated with lower concentrations of Y-27632, IL-1 $\beta$  can eliminate Y-27632-enhanced cell-cell fusion. However, IL-1 $\beta$  was unable to inhibit cell-cell fusion in the presence of higher concentrations of Y-27632 (**Fig. S12C**). Immunofluorescence results showed that although IL-1 $\beta$  induced actin bundles inhibited cell-cell fusion (**Fig. S12D, top panel**), higher concentrations of ROCK inhibitor Y-27632 treatment prevented the formation of IL-1 $\beta$ -induced actin bundles at cell-cell junctions, promoting membrane fusion and cytoplasmic exchange between S-expressing cells and ACE2-expressing cells, which restored syncytia formation (**Fig. S12D, bottom panel**). Furthermore, we verified that IL-1 $\beta$  was unable to reduce S2' cleavage and N protein in the presence of Y-27632 in authentic SARS-CoV-2 infected Caco-2 (**Fig. 5F**), Calu-3 cells (**Fig. 5G**) and human lung cells (**Fig. 5H**). Immunofluorescence results also confirmed that the elimination of IL-1 $\beta$  induced actin bundles by Y-27632 in Caco-2 (**Fig. 5I**) and Calu-3 cells (**Fig. 5J**). These results indicated that preventing the formation of RhoA/ROCK mediated actin bundles at cell-cell junction promotes SARS-CoV-2 induced cell-cell fusion.

## IL-1 $\beta$ restricts SARS-CoV-2 transmission via induction of actin bundles *in vivo*

To demonstrate the role of IL-1 $\beta$  in controlling SARS-CoV-2 transmission *in vivo*, BALB/c mice were infected with authentic SARS-CoV-2 B.1.351 after IL-1 $\beta$  or IL-1RA+IL-1 $\beta$  pre-treatment (**Fig. S13A**). Interestingly, the results of this experiment showed that in mice with IL-1 $\beta$  treatment, the body weight loss was less than in the control group, while IL-1 $\beta$  was unable to improve body weight in

the presence of IL-1RA (**Fig. S13B**). According to hematoxylin and eosin (H&E) staining, tissue histopathology analysis demonstrated that the mice with IL-1 $\beta$  treatment carry less pulmonary injury compared to the control and IL-1RA+IL-1 $\beta$  group (**Fig. 6A and B**). In addition, the expression level of SARS-CoV-2 N gene in the lung from IL-1 $\beta$  treated mice was significantly lower than in the control and IL-1RA+IL-1 $\beta$  treated mice (**Fig. 6C**). In addition, immunohistochemistry staining showed that the infected area in the epithelial linings of lung tissue was significantly reduced by IL-1 $\beta$  treatment compared to the control and IL-1RA+IL-1 $\beta$  groups (**Fig. 6D and E**), indicating that IL-1 $\beta$  restricted the transmission of SARS-CoV-2 in the lung. Moreover, fluorescence staining showed that SARS-CoV-2 infected lung epithelial cells fused with neighboring cells, promoting viral transmission in the airway epithelial cells, while IL-1 $\beta$  induced the formation of actin bundles to restrict the syncytia formation and further viral transmission (**Fig. 6F**, **Fig. S13C and D**).

**Figure 6**

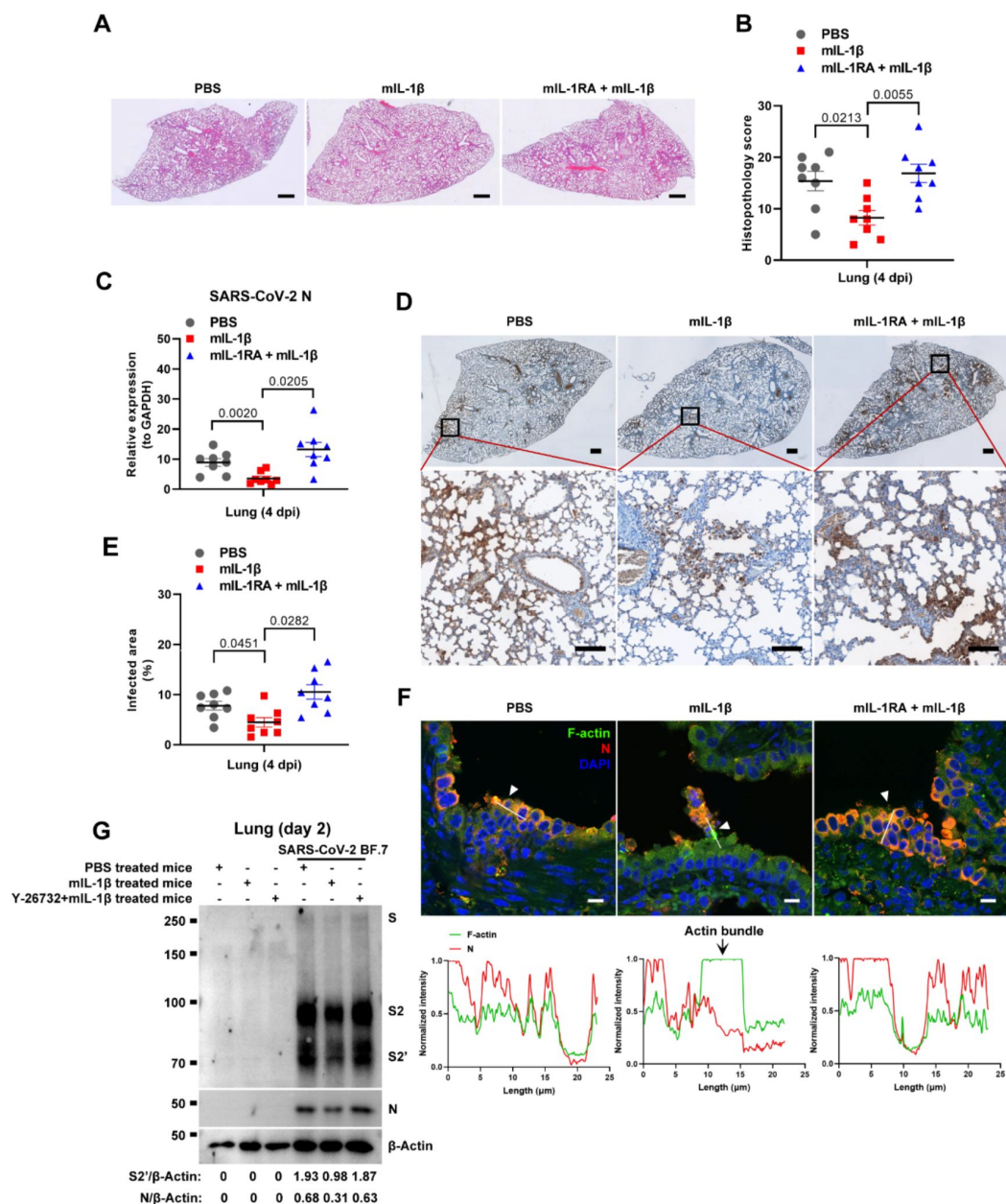


**Fig. 6.**

### IL-1 $\beta$ restricts SARS-CoV-2 transmission via induction of actin bundles in lung tissue.

(A) Schematic for a murine model of authentic SARS-CoV-2 infection, PBS control (n=8); 1  $\mu$ g/kg mIL-1 $\beta$  (n=8); 150  $\mu$ g/kg mIL-1RA + 1  $\mu$ g/kg mIL-1 $\beta$  (n=8) were administered 1 hour before intranasal challenge with  $5 \times 10^4$  FFU of SARS-CoV-2 B.1.351; mice were then intraperitoneal injection with PBS, mIL-1 $\beta$  and mIL-1RA + mIL-1 $\beta$  at 1 dpi and 2 dpi, before sacrificed at 4 dpi. (B) The body weights were assessed daily for weight loss after SARS-CoV-2 infection. (C) qPCR analysis of SARS-CoV-2 N mRNA collected from infected lung tissues at 4 dpi. (D) Immunohistochemistry analysis of SARS-CoV-2 N staining in the lung tissue slices at 4 dpi, scale bars are indicative of 500  $\mu$ m (top panel), 50  $\mu$ m (bottom panel) and images are representative of eight independent experiments. (E) The percentages of SARS-CoV-2 infected area in (D) were quantified. (F) Representative confocal images of F-actin stained with phalloidin-488 and SARS-CoV-2 N in the lung tissue slices at 4 dpi. White arrow heads indicate syncytia formation or infected cells, scale bars are indicative of 10  $\mu$ m and images are representative of three independent experiments (Top). White lines indicate SARS-CoV-2 cell-cell transmission and quantify with fluorescence intensity of F-actin and SARS-CoV-2 N (Bottom). (G) Immunoblots of SARS-CoV-2 S, S2, cleaved S2' and N proteins collected from authentic SARS-CoV-2 BF.7 infected lung tissue cells, which isolated from BALB/c mice treated with PBS, 1  $\mu$ g/kg mIL-1 $\beta$  or 1mg/kg Y-26732 + 1  $\mu$ g/kg mIL-1 $\beta$  at day 2. Blots are representative of three individual experiments. Numbers below the blots indicated the ratio of S2' or N versus  $\beta$ -Actin.

To further verify the function and mechanism of IL-1 $\beta$  in controlling SARS-CoV-2 transmission, we treated BALB/c mice with PBS, IL-1 $\beta$  or ROCK inhibitor Y-26732 + IL-1 $\beta$  (Fig. S14A), then isolated the lung tissue cells for authentic SARS-CoV-2 infection. We found that S2' cleavage and N protein were significantly reduced in IL-1 $\beta$  treated mice compared to control mice at day 2, while Y-26732 treatment abolished the inhibitory effect of IL-1 $\beta$  on S2' cleavage and N protein (Fig. 6G). Of note, the lung tissue cells in IL-1 $\beta$  treated mice remained resistant to SARS-CoV-2 infection at day 7, while the protective effect of IL-1 $\beta$  was abolished by Y-26732 treatment (Fig. S14B).

In addition, we found that IL-1 $\beta$  treated mice have no significant changes in body weight, liver and spleen weight compared to control mice (Fig. S15 A-D), indicating that this dose of IL-1 $\beta$  did not cause toxicity. Of note, we isolated the tissue cells and then infected with authentic SARS-CoV-2, the results showed that S2' cleavage and N protein were significantly reduced in IL-1 $\beta$  treated mice compared to control mice both in isolated lung and intestine tissue cells (Fig. S15 E and F), suggesting that IL-1 $\beta$  may have protective effects on various tissue cells during SARS-CoV-2 infection. Taken together, IL-1 $\beta$  prevents the transmission of SARS-CoV-2 *in vivo* by inducing the formation of actin bundles.

## Discussion

In the present study, we explored the functional roles of innate immune factors against SARS-CoV-2 infection. Notably, IL-1 $\beta$  inhibited various SARS-CoV-2 variants and other beta-coronaviruses spike-induced cell-cell fusion. Mechanistically, IL-1 $\beta$  activates and enriches RhoA to the cell-cell junction between SARS-CoV-2-infected cells and neighboring cells via the IL-1R-mediated signal to initiate actin bundle formation, preventing cell-cell fusion and viral spreading (Fig. S16). These findings revealed a critical antiviral function for pro-inflammatory cytokines to control viral infection.

Elevated IL-1 $\beta$  levels in severe COVID-19 patients is central to innate immune response as it induces the expression of other pro-inflammatory cytokines (Tahtinen et al., 2022). In addition, IL-1 $\alpha$  is also secreted during SARS-CoV-2 infection (Xiao et al., 2021). Of note, several therapeutic



strategies have employed the inhibition of IL-1 signal in an attempt to treat SARS-CoV-2 infection (Huet et al., 2020 [↗](#); Ucciferri et al., 2020 [↗](#)). Intriguingly, although anakinra, a recombinant human IL-1 receptor antagonist, improved clinical outcomes and reduced mortality in severe COVID-19 patients (Cavalli et al., 2020 [↗](#)), it did not reduce mortality in mild-to-moderate COVID-19 patients, and even increased the probability of serious adverse events (Tharaux et al., 2021 [↗](#)). With another note, IL-1 blockade significantly decreased the neutralizing activity of serous anti-SARS-CoV-2 antibodies in severe COVID-19 patients (Della-Torre et al., 2021 [↗](#)). According to our finding that both IL-1 $\beta$  and IL-1 $\alpha$  are able to inhibit SARS-CoV-2-induced cell-cell fusion, inhibition of IL-1 signaling may have abolished the antiviral function of IL-1, thus failing to restrict virus-induced syncytia formation and transmission.

Notably, IL-1 $\beta$  plays a key role in triggering vaccine-induced innate immunity, suggesting that innate immune responses play important roles in the antiviral defense by enhancing the protective efficacy of vaccines (Eisenbarth, Colegio, O'Connor, Sutterwala, & Flavell, 2008 [↗](#); Tahtinen et al., 2022 [↗](#)). In addition, vaccination with *Bacillus Calmette-Guérin* (BCG) has been reported to confer nonspecific protection against heterologous pathogens, including protection against SARS-CoV-2 infection in human and mice (Hilligan et al., 2022 [↗](#); A. Lee et al., 2023 [↗](#); Rivas et al., 2021 [↗](#)). In addition, Lipid nanoparticle (LNP) in mRNA vaccine (Han et al., 2023 [↗](#)) and penton base in adenovirus vaccine (Di Paolo et al., 2009 [↗](#)) can both activate innate immune cells to amplify the protective effect of vaccines, which may also be attributed to IL-1 $\beta$ -mediated inhibition of SARS-CoV-2-induced cell-cell fusion on top of adaptive immune responses induced by the vaccines.

With another note, patients with inherited MyD88 or IRAK4 deficiency have been reported to be selectively vulnerable to COVID-19 pneumonia. It was found that these patients' susceptibility to SARS-CoV-2 can be attributed to impaired type I IFN production, which do not sense the virus correctly in the absence of MyD88 or IRAK4 (García-García et al., 2023 [↗](#)). In our study, MyD88 or IRAK4 deficiency abolished the inhibitory effect of IL-1 $\beta$  on SARS-CoV-2 induced cell-cell fusion, suggesting that these innate immune molecules are critical to contain SARS-CoV-2 infection, and this may be another mechanism accounting for the disease of those patients. Moreover, MyD88 signaling was essential for BCG induced innate and type 1 helper T cell (TH1 cell) responses, and protection against SARS-CoV-2, which is consistent with our fundings.

Of note, cell-cell fusion is not limited to the process of viral infection, both normal and cancerous cells can utilize this physiological process in tissue regeneration or tumor evolution (Delespaul et al., 2020 [↗](#); Powell et al., 2011 [↗](#)). For example, myoblast fusion is the key process of skeletal muscle terminal differentiation, inactivation of RhoA/ROCK signaling is crucial for myoblast fusion (Nishiyama, Kii, & Kudo, 2004 [↗](#)). Our current work revealed that inhibition of RhoA/ROCK signaling promoted virus-induced cell-cell fusion, possibly due to the virus hijacking of such biological process. In turn, activated RhoA/ROCK signaling inhibits virus-induced cell-cell fusion, so it can be targeted for future therapeutic development to control viral transmission. Cell-cell fusion is mediated by actin cytoskeletal rearrangements, the dissolution of F-actin focus is essential for cell-cell fusion; in contrast, syncytia formation cannot proceed if disassembly of actin filaments or bundles is prevented (Doherty et al., 2011 [↗](#); Rodríguez-Pérez et al., 2021 [↗](#)). We uncovered that preventing actin bundles dissolution inhibited virus-induced cell-cell fusion, and IL-1 $\beta$  induced RhoA/ROCK signal promotes actin bundle formation at cell-cell junctions. As RhoA is ubiquitously expressed by all cell types, it is currently unclear whether IL-1-mediated RhoA activation is specific towards viral infection-associated cytoskeleton modification, or may regulate other RhoA-related processes, which is a limitation of the current work and remains to be investigated in future.

In summary, this study demonstrated the function and mechanism of IL-1 $\beta$  in inhibiting SARS-CoV-2 induced syncytia formation, and highlighted the function of innate immune factors including cytokines against coronaviruses transmission, thus provide potential therapeutic targets for viral

control.

## Materials and Methods

### Reagents and plasmids

The antibodies used for immunoblotting include: rabbit anti-SARS-CoV-2 S2 (Sino Biological, 40590-T62, 1:2000), mouse anti-SARS-CoV-2 N (Sino Biological, 40143-MM05, 1:1000), rabbit anti-ACE2 (Proteintech, 21115-1-AP, 1:2000), rabbit anti-MERS-CoV S2 (Sino Biological, 40070-T62, 1:1000), rabbit anti-MyD88 (Cell Signaling Technology, 4283, 1:1000), rabbit anti-TRAF6 (Abcam, ab33915, 1:5000), rabbit anti-TAK1 (Cell Signaling Technology, 4505, 1:1000), mouse anti-Myc-Tag (Abclonal, AE010, 1:2000), HRP-conjugated  $\beta$ -tubulin (Abclonal, AC030, 1:5000), mouse anti- $\beta$ -actin (Proteintech, 66009-1-Ig, 1:5000), anti-rabbit/anti-mouse (Jackson Immuno Research, 111-035-003, 1:5000). The antibodies and reagents used for immunofluorescence include: rabbit anti-SARS-CoV-2 S2 (Sino Biological, 40590-T62, 1:200), mouse anti-SARS-CoV-2 N (Sino Biological, 40143-MM05, 1:200), rabbit anti-ACE2 (Proteintech, 21115-1-AP, 1:200), mouse anti-HA-Tag (Abclonal, AE008, 1:200). Actin-Tracker Green-488 (Beyotime, C2201S, 1:100), goat  $\alpha$ -mouse IgG-555 (Invitrogen, A-21424, 1:400) and goat  $\alpha$ -rabbit IgG-647 (Invitrogen, A-21236, 1:400), DAPI (Abcam, ab228549, 1:2000) and antifade mounting medium (vectorlabs, H-1400-10). Purified LTA from *S. aureus* (Invitrogen, tlr-pslta), Pam3CSK4 (Invitrogen, tlr-pms), Peptidoglycan from *S. aureus* (Sigma-Aldrich, 77140), LPS (Invitrogen, tlr-eklps), TPCA1 (Selleck, S2824), 5Z-7-Oxozeaenol (Sigma-Aldrich, O9890), IRAK1/4 inhibitor (Selleck, S6598), Y-27632 (Selleck, S6390). Inhibitors were dissolved in dimethyl sulfoxide (DMSO, Sigma-Aldrich, D2650), and DMSO was added as solvent control. Recombinant human IL-1 $\alpha$  (200-01A), human IL-1 $\beta$  (200-01B), mouse IL-1 $\beta$  (211-11B), human IL-1RA (200-01RA), human IL-6 (200-06) and human IL-8 (200-08M) were purchased from Peprotech. mouse IL-1RA (769706) was purchased from BioLegend. IL-1 $\beta$  concentrations in supernatants from THP-1 and PBMCs were determined using ELISA kits, according to the manufacturer's instructions (R&D Systems, DY201). RhoA pull-down activation assay Biochem Kit (BK036-S) was purchased from Cytoskeleton, Inc. Collagenase, type I (17100017) was purchased from Gibco and B-Ali Growth Media (00193516) was purchased from Lonza Bioscience.

SARS-CoV-2 spike (Wuhan-Hu-1, GenBank: QHD43419.1) was homo sapiens codon-optimized and generated *de novo* into pVAX1 vector by recursive polymerase chain reaction (PCR). WT, Alpha, Beta and Delta variants containing point and deletion mutations were generated using stepwise mutagenesis using spike construct containing the truncated 19 amino acids at the C-terminal (CTA19). The latest human codon optimized Omicron was purchased from Genescripts, and subcloned into the pVAX1 backbone with CTA19 for comparison. Human ACE2 assembled in a pcDNA4.0 vector was used for transient expression of ACE2. GFP-AHPH (Addgene plasmid # 71368; <http://n2t.net/addgene:71368>; RRID: Addgene\_71368) and pRK5myc RhoA L63 (Addgene plasmid # 15900; <http://n2t.net/addgene:15900>; RRID: Addgene\_15900) were from Addgene.

### Cell culture and stimulation

HEK293T cells were purchased from the National Science & Technology Infrastructure (NSTI) cell bank ([www.cellbank.org.cn](http://www.cellbank.org.cn)). Caco-2 cells (catalog no. SCSP-5027) were obtained from Cell Bank/Stem Cell Bank, Chinese Academy of Sciences. Vero E6-ACE2 and Calu-3 cells were gifted from Prof. Dimitri Lavillette (Applied Molecular Virology Laboratory, Discovery Biology Department, Institut Pasteur Korea). HEK293T and Vero E6-ACE2 were cultured in Gibco Dulbecco's Modified Eagle Medium (DMEM) (GE Healthcare) supplemented with 10% fetal bovine serum (FBS) (Sigma) and 1% Penicillin/streptomycin (P/S) (Life Technologies) at 37°C with 5% CO<sub>2</sub> in a humidified incubator. Human colon epithelial carcinoma cell line Caco-2 and human lung cancer cell line Calu-3 cells were cultured in Minimum Essential Medium (MEM) supplemented with 10% FBS, 1% non-essential amino acids and 1% P/S at 37°C with 5% CO<sub>2</sub> in a humidified incubator. Human monocytic cell line THP-1 was cultured in Roswell Park Memorial Institute



(RPMI) 1640 supplemented with 10% FBS, 1% P/S and 50  $\mu$ M 2-ME at 37°C with 5% CO<sub>2</sub> in a humidified incubator. All cells were routinely tested for mycoplasma contamination; passages between 4<sup>th</sup> to 25<sup>th</sup> were used. Human PBMCs were isolated from the peripheral blood of healthy donors (Shanghai Blood Center). This study was performed in accordance with the International Ethical Guidelines for Biomedical Research Involving Human Subjects and the principles expressed in the Declaration of Helsinki. Briefly, fresh human PBMCs were separated using Ficoll-Paque PLUS reagent (cytiva, 17144003) at 1200 g for 10 min at room temperature with SepMate™-50 (SepMate, 86450). PBMCs were washed three times with filtered PBS containing 0.5% BSA and 2 mM EDTA. PBMCs was counted and resuspended in RPMI 1640 medium supplemented with 1% FBS and 1% P/S.

For stimulation, THP-1 cells were seeded at  $2 \times 10^6$  cells per ml in FBS free RPMI 1640 and PBMCs were seeded at  $1 \times 10^7$  cells per ml in 1% FBS RPMI 1640, then stimulated with LTA (10  $\mu$ g/ml), Pam3CSK4 (1  $\mu$ g/ml), PGN (2  $\mu$ g/ml), LPS (1  $\mu$ g/ml) for 24 hours, cell culture supernatants were collected after centrifugation at 2000 g for 5 min for subsequent experiments.

## Transient transfection and cell-cell fusion assays

For transient transfections, HEK293T cells were seeded in flat bottom 24-well plates at  $0.5 \times 10^6$  cells /mL overnight. 250 ng plasmids encoding SARS-CoV-2 spike mutants or ACE2 variants were packaged in Lipofectamine 2000 (Life technologies) and transfected for 24 hours. For luciferase assays, S-mediated membrane fusion, a *Cre-loxp* Firefly luciferase (*Stop-Luc*) co-expression system was introduced to enable the detection of DNA recombination events during cell-cell-cell fusion. 200 ng Cre plasmids were co-transfected into S-HEK293T cells and 200 ng *Stop-Luc* plasmid were co-transfected into  $\pm$ ACE2-HEK293T cells, respectively. For visualization of syncytia formation, 100 ng ZsGreen plasmid was co-transfected with spike variants. HEK293T cells in the 24-well plates were then detached using ice-cold calcium-free PBS in the absence of trypsin and centrifuged at 600 g for 4 min.

For cell-cell fusion assays, cell pellets were resuspended into complete DMEM and mixed with control HEK293T cells, or HEK293T-ACE2, Vero E6-ACE2 or Calu-3 cells at 1:1 ratio before adhesion to the 48-well or 96-well plates, cell mixes were incubated for 16 hours at 37°C. Quantification of cell-cell-cell fusion was performed by measuring luciferase expression as relative luminescence units (RLU) 1 min by mixing cell lysates with the Steady-Glo luciferase substrate (E2520, Promega) on a Synergy H1 plate reader (Biotek). Fluorescent images showing syncytia formation were captured at endpoint using a 10x objective and 12-bit monochrome CMOS camera installed on the IX73 inverted microscope (Olympus). Attached cells and syncytia were lysed in a NP-40 lysis buffer containing 0.5% (v/v) NP-40, 25 mM Tris pH 7.3, 150 mM NaCl, 5% glycerol and 1x EDTA-free protease inhibitor cocktail (PIC) (Roche).

## Immunoblotting

Tissue culture plates containing adherent syncytia and cell mixes were directly lysed on ice in 2x reducing Laemmli loading buffer before boiled at 95°C for 5 min. Protein samples were separated by standard Tris-glycine SDS-PAGE on 7.5% or 9.5% Tris-glycine polyacrylamide gels. Proteins were then transferred onto 0.45  $\mu$ m PVDF membranes (Millipore) for wet transfer using Towbin transfer buffer. All membranes were blocked in PBS supplemented with 0.1% Tween20 (PBST) and 2.5% bovine serum albumin (BSA) or 5% non-fat dry milk, before overnight incubation in primary antibodies at 4°C. Blots were labelled with HRP-tagged secondary antibodies (Jackson ImmnuoResearch) and visualized with PicoLight substrate enhanced chemiluminescence (ECL) solution (Epizyme Scientific). Immunoblot images were captured digitally using a 5200 chemiluminescent imaging system (Tanon) with molecular weight markers indicated.

## Real time PCR

HEK293T cells of  $0.5 \times 10^6$  cells/mL were inoculated in 24 wells overnight. After the cells were about 80% covered, the specified stimulant was added, washed with PBS for three times, and 1 mL TRIzol Reagent (15596018; Thermo Fisher Scientific) was added for full lysis at room temperature for 5 min, add 250  $\mu$ L chloroform fully mixed at room temperature for 5 min, centrifuge at 10000 r/min, centrifuge at 4°C for 10 min. Carefully remove the aqueous phase using a pipette. Leave behind some of the aqueous phase (about 1 mm above DNA layer to prevent DNA contamination). Place in another 1.5 mL Eppendorf tube. Add 550  $\mu$ L isopropanol to the aqueous phase and mix gently. Leave at -20°C for 30 min. 14000 r/min, centrifuge at 4°C for 20 min, wash with 75% ethanol twice. Dissolve in 30  $\mu$ L DEPC water. Then reverse transcribed to cDNA using a GoSript Reverse Transcription kit (Promega). Real-time PCR was performed using SYBR Green Realtime PCR Master Mix (TOYOBO) on ABI QuantStudio 6 flex Real-time PCR System (Thermo Fisher Scientific). The RT-qPCR Primer sequences for targeting respective genes are displayed in Table S1. Target genes Relative quantification were normalized to GAPDH as relative unit (RU) via formula.

## CRISPR/Cas9-Mediated Gene Targeting

Gene-deficient THP-1 or HEK293T cells were generated using CRISPR/Cas9-mediated gene targeting technology. Briefly, LentiCRISPR v2 (52961; addgene) containing sgRNA specifically targeting indicated genes were constructed. The sgRNA sequences for targeting respective genes are displayed in Table S2. The Lentiviral particles were produced in HEK293T cells by transfection with LentiCRISPR v2-sg gene, psPAX2, VSV-G at 2:1.5:1 ratio using Lipofectamine 2000. The lentiviral particles were then used to infect THP-1 or HEK293T cells. One day post infection, the cells were subjected to puromycin selection at a concentration of 2  $\mu$ g/ml for 72 hours. Surviving cells were subjected to limiting dilution and seed in 96-well plates to obtain single clones stably knocking out respective genes.

## RhoA pull-down assay

After 1 ng/mL IL-1 $\beta$  treatment for 30 min, place culture vessel on ice, aspirate media, wash with ice cold PBS. Aspirate off PBS. Tilt plates on ice for an additional 1 min to remove all remnants of PBS. Residual PBS will adversely affect the assay. Lysis cells in an ice-cold cell lysis buffer with protease inhibitor cocktail. Harvest cell lysates with a cell scraper. Transfer lysates into the pre-labeled sample tubes on ice. Immediately clarify by centrifugation at 10000 g, 4°C for 1 min. Save 20  $\mu$ L of lysate for total RhoA. For pulldown assay, add 600  $\mu$ g total cell protein to 10  $\mu$ L rhotekin-RBD beads, then incubate at 4°C on a rotator for 1 hour. Pellet the rhotekin-RBD beads by centrifugation at 5000 g at 4°C for 1 min. Very carefully remove 90% of the supernatant, then wash the beads once with 500  $\mu$ L each of Wash Buffer. Pellet the rhotekin-RBD beads by centrifugation at 5000 g at 4°C for 3 min. Very carefully remove the supernatant. Add 20  $\mu$ L of 2x Laemmli sample buffer to each tube and thoroughly resuspend the beads. Boil the bead samples for 2 min. The samples were analyzed by Immunoblots.

## Immunostaining and confocal microscopy

HEK293T cells were seeded overnight onto sterilized poly-D-lysine (100  $\mu$ g/mL) (Beyotime, ST508) treated 12 mm coverslips (fisher scientific, 1254580) in 24-well plates. After transfection with spike mutants, cells were washed with PBS once before fixed with 4% (w/v) paraformaldehyde (PFA) for 20 min. Then, cells were washed twice with PBS and permeabilized by 0.1% Triton at room temperature for 10 min. Next, cells were washed twice with PBS and blocked with Immunol Staining Blocking Buffer (Beyotime, P0102) at room temperature for 1 hour. Primary antibodies were incubated at room temperature for 1 hour. Coverslips were then washed twice with PBS before incubation with Actin-Tracker Green-488 or second antibodies for 1 hour at room temperature. Coverslips were washed twice with PBS before DAPI staining for 10 min. Coverslips were washed twice with PBS before mounted in antifade mounting medium. Fluorescent images

covering various areas on the coverslips were captured at 12-bit depth in monochrome using a 100x oil immersion objective on the Olympus SpinSR10 confocal microscope and subsequently processed using imageJ software (NIH) with scale bars labeled.

## Authentic SARS-CoV-2 Infection of cells

All experiments involving authentic SARS-CoV-2 virus *in vitro* were conducted in the biosafety level 3 (BSL3) laboratory of the Shanghai municipal center for disease control and prevention (CDC). The experiments and protocols in this study were approved by the Ethical Review Committee of the Shanghai CDC. Briefly, HEK293T-ACE2 or Caco-2 cells were seeded into 24-well or 96-well plates at a density of  $4 \times 10^5$  cells per mL overnight, then pre-treated cells with different treatments for 1 hour before infected with 0.5 multiplicity of infection (MOI) Delta or WT authentic SARS-CoV-2 (B.1.617.2 and Wuhan-Hu-1) for 24 hours. Calu-3 cells were seeded into 24-well or 96-well plates at a density of  $4 \times 10^5$  cells per mL overnight, infected with 0.5 MOI WT authentic SARS-CoV-2 for 1 hour, then washed with PBS before treated cells with different treatments for 24 hours. Brightfield images were captured to indicate the syncytia formation, cell lysates were collected for spike S2' cleavage and N protein immunoblots.

For mice tissue cells, specific pathogen-free 6-week-old female BALB/c mice were lightly anesthetized with isoflurane and intranasal with PBS, mIL-1 $\beta$  (1  $\mu$ g/kg) or Y-26732 (1 mg/kg) + mIL-1 $\beta$  (1  $\mu$ g/kg) at day 0, then mice were Intraperitoneal injection with PBS, mIL-1 $\beta$  (1  $\mu$ g/kg) or Y-26732 (1 mg/kg) + mIL-1 $\beta$  (1  $\mu$ g/kg) at day 1 and 2. At day 7, mice were anesthetized by intraperitoneal injection of Avertin (2,2,2-tribromoethanol, Sigma-Aldrich), then the thoracic cavity and abdominal cavity of the mice were opened, an outlet was cut in the left ventricle of the mice, and then the right ventricle of the mice was perfused with phosphate buffer saline (PBS) through the pulmonary artery to remove blood cells in the lung. Next, the lung digestive solution with HBSS 1mL, 1 mg/mL collagenase IA, DnaseI (200 mg/mL; Roche), DispaseII (4 U/mL; Gibco) and 5% FBS was injected into the lung cavity; and the intestine digestive solution containing DMEM 10mL, 1  $\mu$ M DTT, 0.25  $\mu$ M EDTA and 5% FBS, then peeled off the lung or intestine organs, and digested for 30 min with shaking at 37°C. After digestion, the cells were resuspended in DMEM supplemented with 10% FBS and 1% P/S, subsequently infected cells with 1 MOI authentic SARS-CoV-2 B.1.351 or BF.7 for 24 hours. All procedures were conducted in compliance with a protocol approved by the Institutional Animal Care and Use Committee (IACUC) at Shanghai Institute of Immunity and Infection, Chinese Academy of Sciences.

For human lung cells, the human lung tissues were cut into small pieces of about 2mm and washed three times with HBSS solution containing 1% PS, digested with collagenase type I (100 mg+50 mL PBS) in an incubator at 37°C for 4 hours. Then filtered through a 70  $\mu$ m filter and centrifuged at 500 g for 5 min at room temperature. Lysed with 3 mL Red Blood Cell Lysis Buffer for 5min at room temperature, and then centrifuged at 500 g for 5 min at room temperature, washed twice with HBSS solution containing 1% PS. Human lung cells were resuspended in B-ALI Growth Media and seeded into 96-well plates at a density of  $4 \times 10^5$  cells per mL overnight, infected with 0.5 MOI WT authentic SARS-CoV-2 for 1 hour, then washed with PBS before treated cells with different treatments for 24 hours. The experiments and protocols were approved by the Ethical Review Committee of the Shanghai CDC.

## Authentic SARS-CoV-2 infection of BALB/c mice

Specific pathogen-free 6-week-old female BALB/c mice were lightly anesthetized with isoflurane and intranasal with PBS, mIL-1 $\beta$  (1  $\mu$ g/kg) or mIL-1RA (150  $\mu$ g/kg) + mIL-1 $\beta$  (1  $\mu$ g/kg) for 1 hour, then intranasal challenge with  $5 \times 10^4$  FFU of SARS-CoV-2 B.1.351. For booster injection, mice were Intraperitoneal injection with PBS, mIL-1 $\beta$  (1  $\mu$ g/kg) or mIL-1RA (150  $\mu$ g/kg) + mIL-1 $\beta$  (1  $\mu$ g/kg) at 1- and 2-days post infection (dpi). Mice were monitored daily for weight loss. Lungs were removed into trizol or 4% PFA at 4 dpi. All protocols were approved by the Institutional Animal Care and Use Committee of the Guangzhou Medical University.

## Pulmonary histopathology

Lungs were collected from mice infected by SARS-CoV-2 at 4 dpi and fixed in 4% PFA (Bioss) for 12 hours followed by dehydrating, embedded in paraffin for sectioning, then stained with hematoxylin and eosin (H&E), immunohistochemistry (IHC) or immunofluorescence (IF). H&E and IHC analyzed by PerkinElmer Vectra 3, IF analyzed by Olympus SpinSR10 confocal microscope. The pathological scores were judged according to this paper ([Curtis, Warnock, Arraj, & Kaltreider, 1990](#) [↗](#)).

## Statistics analysis

Bar graphs were presented as mean values  $\pm$  standard error of mean (SEM) with individual data points. All statistical analyses were carried out with the Prism software v8.0.2 (GraphPad). Data with multiple groups were analyzed using matched one-way ANOVA followed by Sidak's post hoc comparisons. Statistical significance P values were indicated between compared groups and shown on Figures.

## Author Contributions

Conceptualization, X.Z., S.Y. and G.M.; Methodology, X.Z., S.Y., Y.J. and G.M.; Investigation, X.Z., S.Y., Y.Z., K.Y., Y.G., Me.C., D.D., Y.L., J.M., X.C., Y.Y., X.W., Y.J. and J.Z.; Writing – Original Draft, X.Z., S.Y.; Writing – Review & Editing, X.Z., S.Y., Y.J. and G.M.; Funding Acquisition, Y.Z., Y.J., M.C. J.Z and G.M.; Resources, Y.J., M.C. J.Z and G.M.; Supervision, G.M.

## Competing Interest Statement

Authors declare that they have no competing interests.

## Acknowledgements

We thank Qihong Guo, Prof. Dimitri Lavillette and Prof. Gary Wong for their experimental supports and key reagents used in this work. This study is supported by grants from Natural Science Foundation of China (92269202, 82825001, 92054104), National Key R&D Program of China (2022YFC2304700, 2022YFC2303200, 2022YFC2303502), Three-Year Initiative Plan for Strengthening Public Health System Construction in Shanghai (2023-2025) Key Discipline Project (GWVI-11.1-09), as well as the Shanghai Municipal Science and Technology Major Project (2019SHZDZX02). Guangdong Basic and Applied Basic Research Foundation (2023A1515010152) and Young Scientists Fund of the Guangzhou National Laboratory (QNPG23-03).

## References

1. Arabi Y. M., Mandourah Y., Al-Hameed F., Sindi A. A., Almekhlafi G. A., Hussein M. A., Fowler R. A. (2018) **Corticosteroid Therapy for Critically Ill Patients with Middle East Respiratory Syndrome** *Am J Respir Crit Care Med* **197**:757–767 <https://doi.org/10.1164/rccm.201706-1172OC>
2. Barnett K. C., Xie Y., Asakura T., Song D., Liang K., Taft-Benz S. A., Ting J. P. (2023) **An epithelial-immune circuit amplifies inflammasome and IL-6 responses to SARS-CoV-2** *Cell Host Microbe* **31**:243–259 <https://doi.org/10.1016/j.chom.2022.12.005>
3. Belouzard S., Chu V. C., Whittaker G. R (2009) **Activation of the SARS coronavirus spike protein via sequential proteolytic cleavage at two distinct sites** *Proc Natl Acad Sci U S A* **106**:5871–5876 <https://doi.org/10.1073/pnas.0809524106>
4. Blanco-Melo D., Nilsson-Payant B. E., Liu W. C., Uhl S., Hoagland D., Møller R., tenOever B. R. (2020) **Imbalanced Host Response to SARS-CoV-2 Drives Development of COVID-19** *Cell* **181**:1036–1045 <https://doi.org/10.1016/j.cell.2020.04.026>
5. Bussani R., Schneider E., Zentilin L., Collesi C., Ali H., Braga L., Giacca M. (2020) **Persistence of viral RNA, pneumocyte syncytia and thrombosis are hallmarks of advanced COVID-19 pathology** *EBioMedicine* **61** <https://doi.org/10.1016/j.ebiom.2020.103104>
6. Cavalli G., De Luca G., Campochiaro C., Della-Torre E., Ripa M., Canetti D., Dagna L. (2020) **Interleukin-1 blockade with high-dose anakinra in patients with COVID-19, acute respiratory distress syndrome, and hyperinflammation: a retrospective cohort study** *Lancet Rheumatol* **2**:e325–e331 [https://doi.org/10.1016/s2665-9913\(20\)30127-2](https://doi.org/10.1016/s2665-9913(20)30127-2)
7. Chen L. Y., Zuraw B. L., Liu F. T., Huang S., Pan Z. K (2002) **IL-1 receptor-associated kinase and low molecular weight GTPase RhoA signal molecules are required for bacterial lipopolysaccharide-induced cytokine gene transcription** *J Immunol* **169**:3934–3939 <https://doi.org/10.4049/jimmunol.169.7.3934>
8. Curtis J. L., Warnock M. L., Arraj S. M., Kaltreider H. B (1990) **Histologic analysis of an immune response in the lung parenchyma of mice. Angiopathy accompanies inflammatory cell influx** *Am J Pathol* **137**:689–699
9. Delespaul L., Gélabert C., Lesluyes T., Le Guellec S., Pérot G., Leroy L., Chibon F. (2020) **Cell-cell fusion of mesenchymal cells with distinct differentiations triggers genomic and transcriptomic remodelling toward tumour aggressiveness** *Sci Rep* **10** <https://doi.org/10.1038/s41598-020-78502-z>
10. Della-Torre E., Criscuolo E., Lanzillotta M., Locatelli M., Clementi N., Mancini N., Dagna L (2021) **IL-1 and IL-6 inhibition affects the neutralising activity of anti-SARS-CoV-2 antibodies in patients with COVID-19** *Lancet Rheumatol* **3**:e829–e831 [https://doi.org/10.1016/s2665-9913\(21\)00321-0](https://doi.org/10.1016/s2665-9913(21)00321-0)
11. Di Paolo N. C., Miao E. A., Iwakura Y., Murali-Krishna K., Aderem A., Flavell R. A., Shayakhmetov D. M. (2009) **Virus binding to a plasma membrane receptor triggers interleukin-1 alpha-mediated proinflammatory macrophage response in vivo** *Immunity* **31**:110–121 <https://doi.org/10.1016/j.immuni.2009.04.015>

12. Doherty J. T., Lenhart K. C., Cameron M. V., Mack C. P., Conlon F. L., Taylor J. M. (2011) **Skeletal muscle differentiation and fusion are regulated by the BAR-containing Rho-GTPase-activating protein (Rho-GAP), GRAF1** *J Biol Chem* **286**:25903–25921 <https://doi.org/10.1074/jbc.M111.243030>
13. Dupraz S., Hilton B. J., Husch A., Santos T. E., Coles C. H., Stern S., Bradke F. (2019) **RhoA Controls Axon Extension Independent of Specification in the Developing Brain** *Curr Biol* **29**:3874–3886 <https://doi.org/10.1016/j.cub.2019.09.040>
14. Eisenbarth S. C., Colegio O. R., O'Connor W., Sutterwala F. S., Flavell R. A. (2008) **Crucial role for the Nalp3 inflammasome in the immunostimulatory properties of aluminium adjuvants** *Nature* **453**:1122–1126 <https://doi.org/10.1038/nature06939>
15. García-García A., Pérez de Diego R., Flores C., Rinchai D., Solé-Violán J., Deyà-Martínez À, Rodríguez-Gallego C. (2023) **Humans with inherited MyD88 and IRAK-4 deficiencies are predisposed to hypoxemic COVID-19 pneumonia** *J Exp Med* **220** <https://doi.org/10.1084/jem.20220170>
16. Hadjadj J., Yatim N., Barnabei L., Corneau A., Boussier J., Smith N., Terrier B. (2020) **Impaired type I interferon activity and inflammatory responses in severe COVID-19 patients** *Science* **369**:718–724 <https://doi.org/10.1126/science.abc6027>
17. Han X., Alameh M. G., Butowska K., Knox J. J., Lundgreen K., Ghattas M., Mitchell M. J. (2023) **Adjuvant lipidoid-substituted lipid nanoparticles augment the immunogenicity of SARS-CoV-2 mRNA vaccines** *Nat Nanotechnol* <https://doi.org/10.1038/s41565-023-01404-4>
18. Hilligan K. L., Namasivayam S., Clancy C. S., O'Mard D., Oland S. D., Robertson S. J., Sher A. (2022) **Intravenous administration of BCG protects mice against lethal SARS-CoV-2 challenge** *J Exp Med* **219** <https://doi.org/10.1084/jem.20211862>
19. Huet T., Beaussier H., Voisin O., Jouvesshomme S., Dauriat G., Lazareth I., Hayem G. (2020) **Anakinra for severe forms of COVID-19: a cohort study** *Lancet Rheumatol* **2**:e393–e400 [https://doi.org/10.1016/s2665-9913\(20\)30164-8](https://doi.org/10.1016/s2665-9913(20)30164-8)
20. Karki R., Sharma B. R., Tuladhar S., Williams E. P., Zalduondo L., Samir P., Kanneganti T. D. (2021) **Synergism of TNF- $\alpha$  and IFN- $\gamma$  Triggers Inflammatory Cell Death, Tissue Damage, and Mortality in SARS-CoV-2 Infection and Cytokine Shock Syndromes** *Cell* **184**:149–168 <https://doi.org/10.1016/j.cell.2020.11.025>
21. Lee A., Floyd K., Wu S., Fang Z., Tan T. K., Froggatt H. M., Pulendran B. (2023) **BCG vaccination stimulates integrated organ immunity by feedback of the adaptive immune response to imprint prolonged innate antiviral resistance** *Nat Immunol* <https://doi.org/10.1038/s41590-023-01700-0>
22. Lee N., Allen Chan K. C., Hui D. S., Ng E. K., Wu A., Chiu R. W., Lo Y. M. (2004) **Effects of early corticosteroid treatment on plasma SARS-associated Coronavirus RNA concentrations in adult patients** *J Clin Virol* **31**:304–309 <https://doi.org/10.1016/j.jcv.2004.07.006>
23. Li Z., Li S., Zhang G., Peng W., Chang Z., Zhang X., Wu (2022) **An engineered bispecific human monoclonal antibody against SARS-CoV-2** *Nat Immunol* **23**:423–430 <https://doi.org/10.1038/s41590-022-01138-w>



24. Martínez-Mármol R., Giordano-Santini R., Kaulich E., Cho A. N., Przybyla M., Riyadh M. A., Hilliard M. A. (2023) **SARS-CoV-2 infection and viral fusogens cause neuronal and glial fusion that compromises neuronal activity** *Sci Adv* **9** <https://doi.org/10.1126/sciadv.adg2248>
25. Medzhitov R (2001) **Toll-like receptors and innate immunity** *Nat Rev Immunol* **1**:135–145 <https://doi.org/10.1038/35100529>
26. Nishiyama T., Kii I., Kudo A (2004) **Inactivation of Rho/ROCK signaling is crucial for the nuclear accumulation of FKHR and myoblast fusion** *J Biol Chem* **279**:47311–47319 <https://doi.org/10.1074/jbc.M403546200>
27. Nobes C. D., Hall A (1999) **Rho GTPases control polarity, protrusion, and adhesion during cell movement** *J Cell Biol* **144**:1235–1244 <https://doi.org/10.1083/jcb.144.6.1235>
28. Pfaender S., Mar K. B., Michailidis E., Kratzel A., Boys I. N., V’Kovski P., Thiel V. (2020) **LY6E impairs coronavirus fusion and confers immune control of viral disease** *Nat Microbiol* **5**:1330–1339 <https://doi.org/10.1038/s41564-020-0769-y>
29. Powell A. E., Anderson E. C., Davies P. S., Silk A. D., Pelz C., Impey S., Wong M. H (2011) **Fusion between Intestinal epithelial cells and macrophages in a cancer context results in nuclear reprogramming** *Cancer Res* **71**:1497–1505 <https://doi.org/10.1158/0008-5472.can-10-3223>
30. Priya R., Gomez G. A., Budnar S., Verma S., Cox H. L., Hamilton N. A., Yap A. S (2015) **Feedback regulation through myosin II confers robustness on RhoA signalling at E-cadherin junctions** *Nat Cell Biol* **17**:1282–1293 <https://doi.org/10.1038/ncb3239>
31. Rajah M. M., Bernier A., Buchrieser J., Schwartz O (2022) **The Mechanism and Consequences of SARS-CoV-2 Spike-Mediated Fusion and Syncytia Formation** *J Mol Biol* **434** <https://doi.org/10.1016/j.jmb.2021.167280>
32. Ren X., Wen W., Fan X., Hou W., Su B., Cai P., Zhang Z. (2021) **COVID-19 immune features revealed by a large-scale single-cell transcriptome atlas** *Cell* **184**:1895–1913 <https://doi.org/10.1016/j.cell.2021.01.053>
33. Riento K., Ridley A. J (2003) **Rocks: multifunctional kinases in cell behaviour** *Nat Rev Mol Cell Biol* **4**:446–456 <https://doi.org/10.1038/nrm1128>
34. Rivas M. N., Ebinger J. E., Wu M., Sun N., Braun J., Sobhani K., Arditi M. (2021) **BCG vaccination history associates with decreased SARS-CoV-2 seroprevalence across a diverse cohort of health care workers** *J Clin Invest* **131** <https://doi.org/10.1172/jci145157>
35. Rodríguez-Pérez F., Manford A. G., Pogson A., Ingersoll A. J., Martínez-González B., Rape M (2021) **Ubiquitin-dependent remodeling of the actin cytoskeleton drives cell fusion** *Dev Cell* **56**:588–601 <https://doi.org/10.1016/j.devcel.2021.01.016>
36. Sefik E., Qu R., Junqueira C., Kaffe E., Mirza H., Zhao J., Flavell R. A. (2022) **Inflammasome activation in infected macrophages drives COVID-19 pathology** *Nature* **606**:585–593 <https://doi.org/10.1038/s41586-022-04802-1>

37. Stern S., Hilton B. J., Burnside E. R., Dupraz S., Handley E. E., Gonyer J. M., Bradke F. (2021) **RhoA drives actin compaction to restrict axon regeneration and astrocyte reactivity after CNS injury** *Neuron* **109**:3436–3455 <https://doi.org/10.1016/j.neuron.2021.08.014>
38. Straus M. R., Tang T., Lai A. L., Flegel A., Bidon M., Freed J. H., Whittaker G. R. (2020) **Ca(2+) Ions Promote Fusion of Middle East Respiratory Syndrome Coronavirus with Host Cells and Increase Infectivity** *J Virol* **94** <https://doi.org/10.1128/jvi.00426-20>
39. Sun L., Guan R., Lee I. J., Liu Y., Chen M., Wang J., Chen Z. (2015) **Mechanistic insights into the anchorage of the contractile ring by anillin and Mid1** *Dev Cell* **33**:413–426 <https://doi.org/10.1016/j.devcel.2015.03.003>
40. Tahtinen S., Tong A. J., Himmels P., Oh J., Paler-Martinez A., Kim L., Mellman I. (2022) **IL-1 and IL-1ra are key regulators of the inflammatory response to RNA vaccines** *Nat Immunol* **23**:532–542 <https://doi.org/10.1038/s41590-022-01160-y>
41. Tharaux P.-L., Pialoux G., Pavot A., Mariette X., Hermine O., Resche-Rigon M., Renet S. (2021) **Effect of anakinra versus usual care in adults in hospital with COVID-19 and mild-to-moderate pneumonia (CORIMUNO-ANA-1): a randomised controlled trial** *The Lancet Respiratory Medicine* **9**:295–304 [https://doi.org/10.1016/S2213-2600\(20\)30556-7](https://doi.org/10.1016/S2213-2600(20)30556-7)
42. Ucciferri C., Auricchio A., Di Nicola M., Potere N., Abbate A., Cipollone F., Falasca K. (2020) **Canakinumab in a subgroup of patients with COVID-19** *Lancet Rheumatol* **2**:e457–ee458 [https://doi.org/10.1016/s2665-9913\(20\)30167-3](https://doi.org/10.1016/s2665-9913(20)30167-3)
43. van der Heijden M., Versteilen A. M., Sipkema P., van Nieuw Amerongen G. P., Musters R. J., Groeneveld A. B. (2008) **Rho-kinase-dependent F-actin rearrangement is involved in the inhibition of PI3-kinase/Akt during ischemia-reperfusion-induced endothelial cell apoptosis** *Apoptosis* **13**:404–412 <https://doi.org/10.1007/s10495-007-0173-6>
44. Wang S., Li W., Hui H., Tiwari S. K., Zhang Q., Croker B. A., Rana T. M. (2020) **Cholesterol 25-Hydroxylase inhibits SARS-CoV-2 and other coronaviruses by depleting membrane cholesterol** *EMBO J* **39** <https://doi.org/10.15252/emboj.2020106057>
45. Watanabe N., Kato T., Fujita A., Ishizaki T., Narumiya S (1999) **Cooperation between mDia1 and ROCK in Rho-induced actin reorganization** *Nat Cell Biol* **1**:136–143 <https://doi.org/10.1038/11056>
46. Weber A., Wasiliew P., Kracht M (2010) **Interleukin-1beta (IL-1beta) processing pathway** *Sci Signal* **3** <https://doi.org/10.1126/scisignal.3105cm2>
47. Xiao N., Nie M., Pang H., Wang B., Hu J., Meng X., Hu Z. (2021) **Integrated cytokine and metabolite analysis reveals immunometabolic reprogramming in COVID-19 patients with therapeutic implications** *Nat Commun* **12** <https://doi.org/10.1038/s41467-021-21907-9>
48. Yu S., Zheng X., Zhou B., Li J., Chen M., Deng R., Meng G. (2022) **SARS-CoV-2 spike engagement of ACE2 primes S2' site cleavage and fusion initiation** *Proc Natl Acad Sci U S A* **119** <https://doi.org/10.1073/pnas.2111199119>
49. Yu S., Zheng X., Zhou Y., Gao Y., Zhou B., Zhao Y., Meng G. (2023) **Antibody-mediated spike activation promotes cell-cell transmission of SARS-CoV-2** *PLoS Pathog* **19** <https://doi.org/10.1371/journal.ppat.1011789>

50. Zhou P., Yang X. L., Wang X. G., Hu B., Zhang L., Zhang W., Shi Z. L. (2020) **A pneumonia outbreak associated with a new coronavirus of probable bat origin** *Nature* **579**:270–273 <https://doi.org/10.1038/s41586-020-2012-7>

## Editors

Reviewing Editor

**John Schoggins**

The University of Texas Southwestern Medical Center, Dallas, United States of America

Senior Editor

**John Schoggins**

The University of Texas Southwestern Medical Center, Dallas, United States of America

## Reviewer #1 (Public Review):

Summary:

SARS-CoV-2 infection induces syncytia formation, which promotes viral transmission. In this paper, the authors aimed to understand how host-derived inflammatory cytokines IL-1 $\alpha/\beta$  combat SARS-CoV-2 infection.

Strengths:

First, they used a cell-cell fusion assay developed previously to identify IL-1 $\alpha/\beta$  as the cytokines that inhibit syncytia formation. They co-cultured cells expressing the spike protein and cells expressing ACE2 and found that IL-1 $\beta$  treatment decreased syncytia formation and S2' cleavage.

Second, they investigated the IL-1 signaling pathway in detail, using knockouts or pharmacological perturbation to understand the signaling proteins responsible for blocking cell fusion. They found that IL-1 prevents cell-cell fusion through MyD88/IRAK/TRAF6 but not TAK1/IKK/NF- $\kappa$ B, as only knocking out MyD88/IRAK/TRAF6 eliminates the inhibitory effect on cell-cell fusion in response to IL-1 $\beta$ . This revealed that the inhibition of cell fusion did not require a transcriptional response and was mediated by IL-1R proximal signaling effectors.

Third, the authors identified RhoA/ROCK activation by IL-1 as the basis for this inhibition of cell fusion. By visualizing a RhoA biosensor and actin, they found a redistribution of RhoA to the cell periphery and cell-cell junctions after IL-1 stimulation. This triggered the formation of actin bundles at cell-cell junctions, preventing fusion and syncytia formation. The authors confirmed this molecular mechanism by using constitutively active RhoA and an inhibitor of ROCK.

Diverse Cell types and in vivo models were used, and consistent results were shown across diverse models. These results were convincing and well-presented.

Weaknesses:

As the authors point out in the discussion, whether IL-1-mediated RhoA activation is specific to viral infection or regulates other RhoA-regulated processes is unclear. We would also require high-magnification images of the subcellular organization of the cytoskeleton to appreciate the effect of IL-1 stimulation.

<https://doi.org/10.7554/eLife.98593.1.sa1>

**Reviewer #2 (Public Review):****Summary:**

In this study, Zheng et al investigated the role of inflammatory cytokines in protecting cells against SARS-CoV-2 infection. They demonstrate that soluble factors in the supernatants of TLR-stimulated THP1 cells reduce fusion events between HEK293 cells expressing SARS-CoV-2 S protein and the ACE2 receptor. Using qRT-PCR and ELISA, they demonstrate that IL-1 cytokines are (not surprisingly) upregulated by TLR treatment in THP1 cells. Further, they convincingly demonstrate that recombinant IL-1 cytokines are sufficient to reduce cell-to-cell fusion mediated by the S protein. Using chemical inhibitors and CRISPR knock-out of key IL-1 receptor signaling components in HEK293 cells, they demonstrate that components of the myddosome (MYD88, IRAK1/4, and TRAF6) are required for fusion inhibition, but that downstream canonical signaling (i.e., TAK1 and NFκB activation) is not required. Instead, they provide evidence that IL-1-dependent non-canonical activation of RhoA/Rock is important for this phenotype. Importantly, the authors demonstrate that expression of a constitutively active RhoA alone is sufficient to inhibit fusion and that chemical inhibition of Rock could reverse this inhibition. The authors followed up these in vitro experiments by examining the effects of IL-1 on SARS-CoV-2 infection in vivo and they demonstrate that recombinant IL-1 can reduce viral burden and lung pathogenesis in a mouse model of infection. However, the contribution of the RhoA/Rock pathway and inhibition of fusion to IL-1-mediated control of SARS-CoV-2 infection in vivo remains unclear.

**Strengths:**

- (1) The bioluminescence cell-cell fusion assay provides a robust quantitative method to examine cytokine effects on viral glycoprotein-mediated fusion.
- (2) The study identifies a new mechanism by which IL-1 cytokines can limit virus infection.
- (3) The authors tested IL-1 mediated inhibition of fusion induced by many different coronavirus S proteins and several SARS-CoV-2 strains.

**Weaknesses:**

- (1) The qualitative assay demonstrating S2 cleavage and IL-1 mediated inhibition of this phenotype is extremely variable across the data figures. Sometimes it appears like S2 cleavage (S2') is reduced, while in other figures immunoblots show that total S2 protein is decreased. Based on the proposed model the expectation would be that S2 abundance would be rescued when cleavage is inhibited.
- (2) The text referencing Figure 1H suggests that TLR-stimulated THP-1 cell supernatants "significantly" reduce syncytia, but image quantification and statistics are not provided to support this statement.
- (3) The authors conclude that because IL-1 accumulates in TLR2-stimulated THP1 monocyte supernatants, this cytokine accounts for the ability of these supernatants to inhibit cell-cell fusion. However, they do not directly test whether IL-1 is required for the phenotype. Inhibition of the IL-1 receptor in supernatant-treated cells would help support their conclusion.
- (4) Immunoblot analysis of IL-1 treated HEK293 cells suggests that this cytokine does not reduce the abundance of ACE2 or total S protein in cells. However, it is possible that IL-1 signaling reduces the abundance of these proteins on the cell surface, which would result in a similar inhibition of cell-cell fusion. The authors should confirm that IL-1 treatment of their cells does not change Ace2 or S protein on the cell surface.

(5) In Figure 5A, expression of constitutively active RhoA appears to have profound effects on how ACE2 runs by SDS-PAGE, suggesting that RhoA may have additional effects on ACE2 biology that might account for the decreased cell-cell fusion. This phenotype should be addressed in the text and explored in more detail.

(6) The experiments linking IL-1 mediated restriction of SARS-COV-2 fusion to the control of virus infection in vivo are incomplete. The reported data demonstrate that recombinant IL-1 can restrict virus replication in vivo, but they fall short of confirming that the in vitro mechanism described (reduced fusion) contributes to the control of SARS-CoV2 replication in vivo. A critical piece of data that is missing is the demonstration that the ROCK inhibitor phenocopies IL-1RA treatment of SARS-COV-2 infected mice (viral infection and pathology).

<https://doi.org/10.7554/eLife.98593.1.sa0>